ELSEVIER

Nuclear Instruments and Methods in Physics Research A 401 (1997) 7–44

NUCLEAR INSTRUMENTS & METHODS IN PHYSICS RESEARCH Section A

The CHORUS experiment to search for $\nu_\mu \rightarrow \nu_\tau$ oscillation

CHORUS Collaboration

E. Eskut[a], A. Kayis[a], G. Onengüt[a], R. van Dantzig[b], J. Konijn[b], R.G.C. Oldeman[b], C.A.F.J. van der Poel[b], J.W.E. Uiterwijk[b], J.L. Visschers[b], A.S. Ayan[c], E. Pesen[c], M. Serin-Zeyrek[c], R. Sever[c], P. Tolun[c], M.T. Zeyrek[c], N. Armenise[d], F. Cassol[d], M.G. Catanesi[d], M.T. Muciaccia[d], E. Radicioni[d], S. Simone[d], L. Vivolo[d], D. Eckstein[e,1], P. Lendermann[e,1], A. Meyer-Sievers[e,1], T. Patzak[e], K. Winter[e,1], P. Righini[f], B. Saitta[f], P. Annis[g,2], M. Gruwe[g,3,4], C. Mommaert[g,3,5], M. Vander Donckt[g,4], B. Van de Vyver[g,6], P. Vilain[g,7], G. Wilquet[g,7], E. Di Capua[h], M. Ferroni[h], C. Luppi[h], S. Ricciardi[h,3], Y. Ishii[i], T. Kawamura[i], M. Kazuno[i], S. Ogawa[i], H. Shibuya[i], R. Beyer[j,8], J. Brunner[j], G. Carnevale[j], J.P. Fabre[j], R. Ferreira[j], W. Flegel[j], R. Gurin[j,9], M. de Jong[j], M. Litmaath[j], L. Ludovici[j,10], D. Macina[j,11], R. Meijer Drees[j,12], H. Meinhard[j], E. Niu[j], H. Øverås[j], J. Panman[j], F. Riccardi[j], A. Rozanov[j,13], D. Saltzberg[j], G. Stefanini[j], R. Tzenov[j,14], Ch. Weinheimer[j], H.T. Wong[j], P. Zucchelli[j], J. Goldberg[k], K. Hoepfner[k], H. Chikawa[l], E. Arik[m], I. Birol[m], A.A. Mailov[m], C.H. Hahn[n], H.I. Jang[n], D.C. Kim[n], J.Y. Kim[n], S.N. Kim[n], I.G. Park[n], M.S. Park[n], J.S. Song[n], C.S. Yoon[n], K. Kodama[o], N. Ushida[o], S. Aoki[p], T. Hara[p], G. Brooijmans[q,15], D. Favart[q], G. Grégoire[q], J. Hérin[q,15], V. Lemaitre[q,8], A. Artamonov[r], V. Epstein[r], P. Gorbunov[r], V. Khovansky[r], V. Shamanov[r], V. Smirnitsky[r], D. Bonekämper[s,1], D. Frekers[s,1], D. Rondeshagen[s,1], T. Wolff[s,1], K. Hoshino[t], M. Kobayashi[t], M. Komatzu[t], Y. Kotaka[t], T. Kozaki[t], M. Miyanishi[t], M. Nakamura[t], T. Nakano[t], K. Niu[t], K. Niwa[t], Y. Obayashi[t], O. Sato[t], T. Toshito[t], S. Buontempo[u], L. Casagrande[u], A.G. Cocco[u], N. D'Ambrosio[u], A. Ereditato[u,*], G. Fiorillo[u], F. Garufi[u], F. Marchetti-Stasi[u], M. Messina[u], P. Migliozzi[u], V. Palladino[u], S. Sorrentino[u], P. Strolin[u], K. Nakamura[v], T. Okusawa[v], T. Yoshida[v], A. Capone[w], D. De Pedis[w], S. Di Liberto[w], U. Dore[w], P.F. Loverre[w], A. Maslennikov[w,9], M.A. Mazzoni[w], F. Meddi[w], G. Piredda[w], R. Santacesaria[w], A. di Bartolomeo[x], C. Bozza[x], G. Grella[x], G. Iovane[x], G. Romano[x], G. Rosa[x,16], Y. Sato[y], I. Tezuka[y]

[a] *Çukurova University, Adana, Turkey*
[b] *NIKHEF, Amsterdam, The Netherlands*
[c] *METU, Ankara, Turkey*
[d] *Università di Bari and INFN, Bari, Italy*
[e] *Humboldt Universität, Berlin, Germany*
[f] *Università di Cagliari and INFN, Cagliari, Italy*
[g] *Inter-University Institute for High Energies (ULB-VUB), Brussels, Belgium*

PII S0168-9002(97)00931-5

[h] Università di Ferrara and INFN, Ferrara, Italy
[i] Toho University, Funabashi, Japan
[j] CERN, Geneva, Switzerland
[k] Technion, Haifa, Israel
[l] Kinki University, Higashiosaka, Japan
[m] Bogazici University, Istanbul, Turkey
[n] Gyeongsang National University, Jinju, South Korea
[o] Aichi University of Education, Kariya, Japan
[p] Kobe University, Kobe, Japan
[q] Université Catholique de Louvain, Louvain-la-Neuve, Belgium
[r] Institute for Theoretical and Experimental Physics, Moscow, Russian Federation
[s] Westfälische Wilhelms-Universität, Münster, Germany
[t] Nagoya University, Nagoya, Japan
[u] Università Federico II and INFN, Naples, Italy
[v] Osaka City University, Osaka, Japan
[w] Università La Sapienza and INFN, Rome, Italy
[x] Università di Salerno and INFN, Salerno, Italy
[y] Utsunomiya University, Utsunomiya, Japan

Received 25 March 1997; received in revised form 11 June 1997

Abstract

A new experimental apparatus, designed principally for a high sensitivity search for $\nu_\mu \rightarrow \nu_\tau$ oscillation, has been successfully constructed and made operational by the CHORUS Collaboration for the CERN-WA95 experiment. It consists of a large emulsion target, a scintillating fiber tracker system with optoelectronics read-out, an air-core magnet, a set of trigger hodoscopes, a calorimeter based on the lead/scintillating-fiber technique, and a muon spectrometer. The design, construction and performance of the entire apparatus and of the different detectors are described.

* Correspondence address: Div. PPE, CERN, 1211 Geneva 23, Switzerland.

[1] Supported by the German Bundesministerium für Bildung und Forschung under contract numbers 05 6BU11P and 05 7MS12P.
[2] Supported by Regione autonoma della Sardegna, Italy.

[3] Now at CERN, Geneva, Switzerland.

[4] Fonds pour la Formation a la Recherche dans l'Industrie et dans l'Agriculture.
[5] Interuniversitair Instituut voor Kernwetenschappen.
[6] Nationaal Fonds voor Wetenschappelijk Onderzoek.
[7] Fonds National de la Recherche Scientifique.

[8] Now at DESY, Hamburg, Germany.

[9] CASPUR, Rome, Italy.

[10] On leave of absence from INFN Sezione di Roma, Rome, Italy.

[11] Now at Université de Genève, Geneva, Switzerland.

[12] Now at University of Washington, Seattle, USA.

[13] Now at Université de Marseille, Marseille, France.

[14] On leave of absence from Sofia University, Bulgaria, with support from the Bogazici University, Centre for Turkish–Balkan Physics Research and Applications.

[15] Institut Interuniversitaire des Sciences Nucléaires.

[16] Now at Università La Sapienza and INFN, Rome, Italy.

1. Introduction

Neutrino masses and mixings, if they exist, will have profound implications for particle physics, astrophysics and cosmology [1]. The investigation of these fundamental neutrino properties remains one of the great challenges in experimental particle physics. Reports on the anomalies in measurements of solar, atmospheric and medium-energy accelerator neutrinos, as well as on the observations inferring the existence of cosmological Dark Matter in the Universe, can be explained by invoking massive neutrinos [2]. In this scenario, a high sensitivity search for $\nu_\mu \rightarrow \nu_\tau$ oscillation has great relevance [3].

The principal aim of the CERN-WA95/CHORUS (CERN Hybrid Oscillation Research ApparatUS) experiment [4] is to search for neutrino oscillation in the $\nu_\mu \rightarrow \nu_\tau$ appearance channel with the CERN SPS Wide-Band Neutrino Beam (WBB). The experiment was approved in September 1991 and the construction

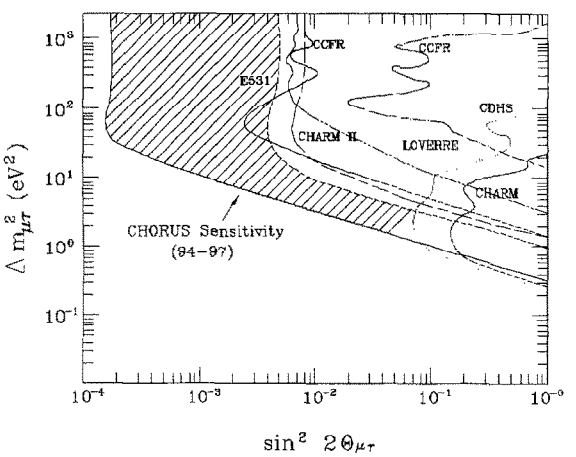

Fig. 1. The $(\sin^2 2\theta_{\mu\tau}, \Delta m^2_{\mu\tau})$ parameter space explored by the CHORUS experiment, together with the regions excluded by previous experiments.

of the detector was completed by November 1993. Physics data taking started in May 1994 and will continue until the end of 1997.

The $\Delta m^2_{\mu\tau}$ versus $\sin^2 2\theta_{\mu\tau}$ parameter space explored by CHORUS, together with regions excluded by previous experiments, is shown in Fig. 1. With four years of data taking, the expected sensitivity is $\sin^2 2\theta_{\mu\tau} \sim 2 \times 10^{-4}$ at large $\Delta m^2_{\mu\tau}$. This measurement would constitute an improvement of more than a factor of twenty over existing limits [5]. The parameter space explored by CHORUS is relevant for the hypothesis of ν_τ as a Dark Matter candidate [6].

In addition, the experiment is sensitive to $\nu_e \rightarrow \nu_\tau$ oscillation, to a level of $\sin^2 2\theta_{e\tau} \sim 10^{-2}$ at large $\Delta m^2_{e\tau}$. It is also expected to contribute to the studies on structure functions and charm physics, using the neutrino beam as a probe.

In this paper the experimental apparatus is described, with particular emphasis given on the design, construction and performance of the different detector subsystems.

2. Conceptual design

In the CHORUS experiment, the signature for $\nu_\mu \rightarrow \nu_\tau$ oscillation is the explicit detection of the vertex in the charged-current (CC) interaction $\nu_\tau N \rightarrow \tau^- X$ and of the subsequent decay topologies of the short-lived τ^- to its daughters ("kink" for one-prong decays, and "star" for three-prong decays), shown schematically in Fig. 2. The principal decay channels of the τ^- which are studied include:

$$\tau^- \rightarrow \mu^- \bar{\nu}_\mu \nu_\tau,$$

$$\tau^- \rightarrow (\text{hadron}^-)(n\pi^0)\nu_\tau,$$

$$\tau^- \rightarrow (\pi^+\pi^-\pi^-)(n\pi^0)\nu_\tau,$$

with branching ratios of 17.8%, 50.4% and 13.8%, respectively. At the typical energies of the CERN Neutrino Beam, the τ leptons produced in the case of oscillation with large Δm^2 have an average flight path of order 1 mm (the mean life of the τ-lepton being 3×10^{-13} s).

CHORUS adopts the "hybrid" approach of combining the emulsion and the electronic detection techniques. The schematic diagram of the CHORUS apparatus is depicted in Fig. 3. The experimental set-up is composed of an emulsion target, a scintillating fiber tracker system, scintillator trigger hodoscopes, an air-core magnet, a lead/scintillator calorimeter, and a muon spectrometer.

The target material consists of a total of 770 kg of nuclear emulsion, where the neutrino interactions are recorded. Nuclear emulsion provides three-dimensional spatial information with an excellent resolution of the order of 1 μm, as well as a high hit density of 300 hits/mm along tracks. They are therefore ideal for the unambiguous detection of short-lived particles. This is crucial to attain the design sensitivity, where the rejection of the events due to $\nu_\mu N$ interactions has to be better than the 10^{-6} level [4]. Reconstruction and analysis of the neutrino events recorded in the emulsion target is carried out by automatic scanning systems.

Downstream of the emulsion target are the electronic detectors. The fiber tracker system provides accurate trajectory predictions back to the emulsion target. The good two-track resolution is crucial for event reconstruction. Together with the air-core magnet, the tracker also measures the charge and momentum of the traversing particles. The calorimeter provides high-resolution measurements for the energies and directions of the hadronic and electromagnetic showers, as well as tracking capabilities.

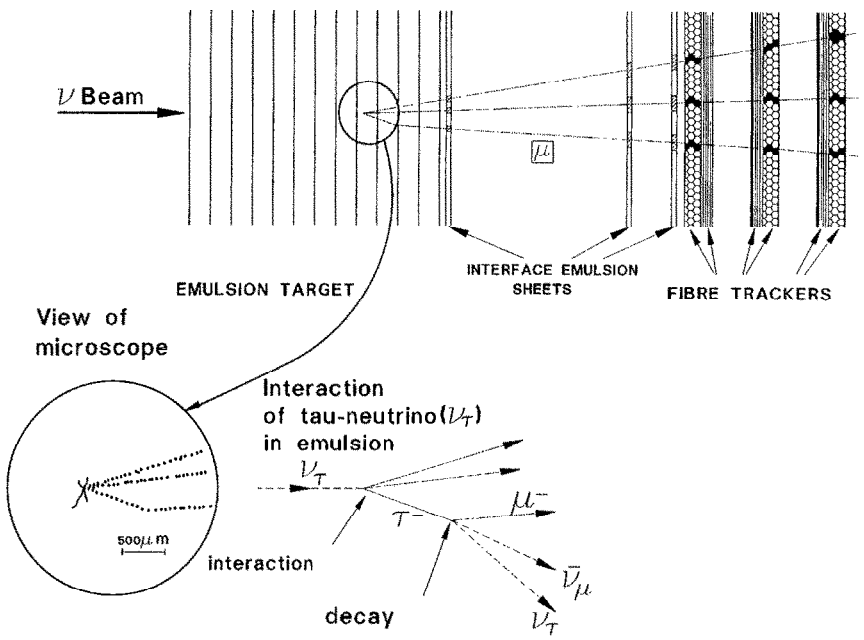

Fig. 2. Schematics of the ν_τ charged-current interaction in the emulsion target, followed by the subsequent decay of the τ^-. The interface emulsion sheets are labelled CS and SS.

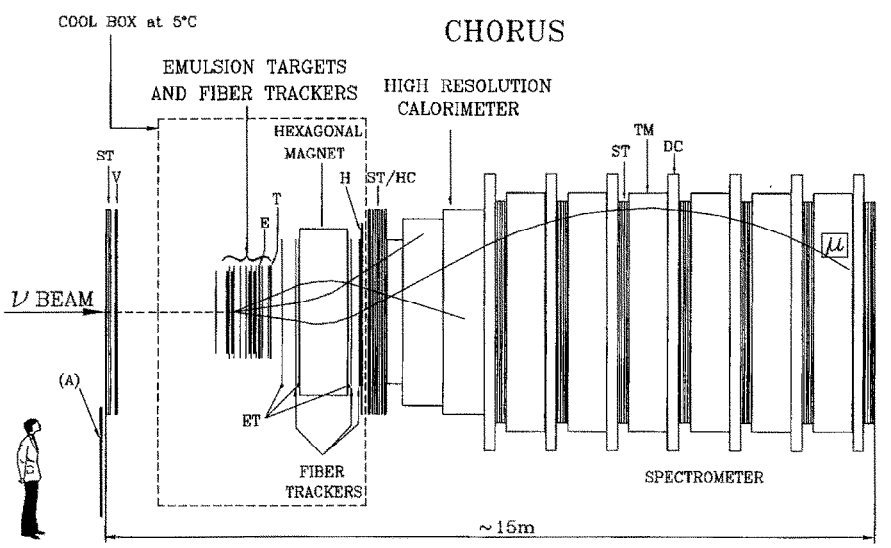

Fig. 3. Schematic diagram (side view) of the CHORUS apparatus. The trigger and veto hodoscopes are denoted by V, A, T, E, H, while ST, TM and DC are the streamer tubes, iron toroidal magnets and the drift chambers, respectively, of the muon spectrometer system. The detector upgrades in 1996 on the emulsion trackers and honeycomb chambers are denoted by ET and HC, respectively. In the actual set-up, individual modules are mounted vertically while the axis of the apparatus is inclined at 42 mrad to match the neutrino beam axis.

The charge and the momentum of the muons are measured by the muon spectrometer system.

The trajectories of charged particles reconstructed by the fiber tracker are traced back into thin interface emulsion-plates. These are placed directly downstream of the emulsion target, where scanning starts. Once track segments are found in these interface plates one can in turn extrapolate with high accuracy into the emulsion target, to locate the vertex positions. This procedure can be performed for a sample of the events. Using the information given by the electronic detectors, events with kinematics close to the ν_τ charged-current interactions are pre-selected out of the overwhelming ν_μ interactions. Consequently, the required scanning time for the emulsions is reduced. Once events with the typical decay topologies are located in the emulsion target, further kinematical and particle identification considerations provide the constraints to discriminate the τ^- signals from the background events with similar topologies, such as those due to charm decays or to the elastic scattering of pions.

3. The neutrino beam

The West Area Neutrino Facility (WANF) of the CERN SPS provides a beam of ν_μ with energies mostly above threshold for ν_τ CC interactions. Protons are accelerated by the SPS to an energy of 450 GeV with a cycle of 14.4 s. They are extracted in two 6 ms long spills separated in time by 2.7 s, onto a beryllium target, producing mainly pions and kaons. Neutrinos originate from their decays in flight, mostly in a 289 m long vacuum tunnel. In this paper we will refer to the "interspill" defined as the time interval between the first and the second spill ($\sim$2.7 s), and to the "interburst" as the interval between the second spill and the first one of the following SPS cycle ($\sim$12 s). The time structure of the SPS cycle is shown in Fig. 4.

A second experiment on $\nu_\mu \rightarrow \nu_\tau$ oscillation, CERN-WA96/NOMAD [7] is running in the same neutrino beam line downstream of the CHORUS experiment. A description of the WANF in the wide band horn-focused configuration adopted for the CHORUS and NOMAD experiments can be found in [8], and its layout is shown in Fig. 5.

A major reconstruction of the WANF took place in 1992 and 1993. The main modifications are as follows. The electronics, data aquisition and control system of the Neutrino Flux Monitoring system (NFM) were replaced with modern equipment. The target and the focusing section of the beam line were completely dismantled and cleared of radioactive waste. A new target station was installed with improved radiation containment properties. The geometry of the beryllium target was left unchanged with 11 rods of 10 cm length (separated by 9 cm gaps) and of 3 mm diameter, larger than the full width of the proton beam. A new tapered small-angle collimator matches the parent beam to the horn aperture.

A larger number of detected ν_τ CC events can be obtained raising the average neutrino energy: the cross-section increases rapidly with energy (above a threshold of about 3.5 GeV) and so does the detection efficiency. A larger average neutrino energy was achieved by increasing the distance from the target of both focusing lenses by about 8 m. The first and the second lens (called the "horn" and the "reflector", respectively) are now 20 and 90 m downstream of the target. Two successive helium-filled tubes of 80 cm diameter and total length of about 100 m were inserted in the flight path between the horn and the reflector and between the reflector and the decay tunnel. This allows to reduce the absorption of parent mesons whose decays give rise to the neutrinos.

Positive (negative) mesons are focused (defocused) by the horn and the reflector. A few percent contamination of muon antineutrinos is nevertheless present in the beam owing to the decay of negative parent particles. In order to reduce this background source, a new large angle collimator was introduced in front of the reflector to intercept defocused negative parents before their decay.

The neutrino beam has an upward slope of 42 mrad. The axis of the CHORUS apparatus is correspondingly inclined with respect to the floor of the experimental hall so to coincide with the neutrino beam axis. However, individual detector modules are installed vertically.

The rebuilt neutrino facility has operated since the end of 1993. Its complete re-alignment is described in Ref. [9]. The improved cooling system enables the beryllium target to sustain high proton intensities

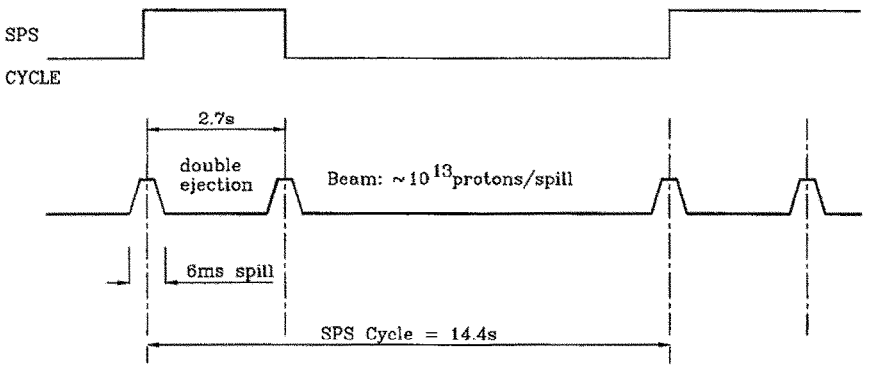

Fig. 4. The timing structure of the CERN SPS cycle and the Wide-Band Neutrino Beam.

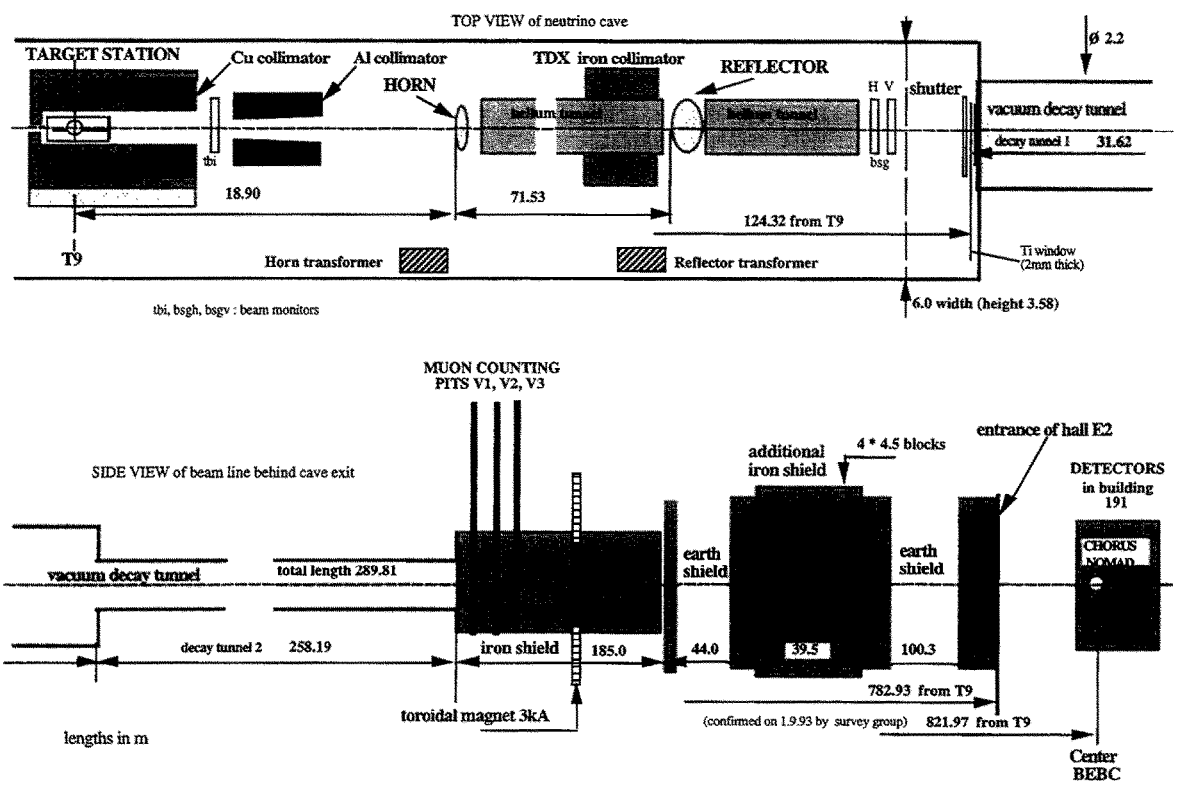

Fig. 5. The layout of the CERN Wide Band Neutrino Beam.

Table 1
The relative composition of the CERN Wide Band Neutrino Beam at the CHORUS experiment

Neutrino species	Relat. abundance	$\langle E \rangle$ (GeV)
ν_μ	100%	26.9
$\bar{\nu}_\mu$	5.6%	21.7
ν_e	0.7%	47.9
$\bar{\nu}_e$	0.17 %	35.3

(up to the record value of 1.5×10^{13} for each of the two spills).

Abundances and mean energies of all neutrino species were measured, together with the absolute muon neutrino event rate, in the previous CHARM II experiment [11]. The corresponding values at the CHORUS detector, which has smaller lateral dimension and is situated about 60 m upstream, can be estimated from this measurement, with the help of a Monte Carlo simulation. The results are summarized in Table 1. The estimated muon event rate in CHORUS is 2.1×10^{-14} CC events per proton. The ν_τ contamination of the beam, the irreducible background for the $\nu_\mu \rightarrow \nu_\tau$ oscillation search, is expected to be at the (negligible) level of ν_τ CC/ν_μ CC ~ 3–4×10^{-6} [10], corresponding to ~ 0.1 background events for the total CHORUS data taking.

The modifications introduced to the neutrino beam line, however, affect the values shown in Table 1. Fig. 6 shows the energy spectra of the different components of the neutrino beam intercepted by the CHORUS emulsions ($1.4 \times 1.4\,m^2$ area) as predicted by a full Monte Carlo simulation of the modified beam line. They should be taken only as a preliminary indication, in view of the uncertainties affecting the neutrino beam simulation, mostly due to the limited knowledge of the yield of pions and kaons from hadronic interactions in the target and in other materials. A measurement at the CHORUS location in the modified beam line is necessary and is currently in progress.

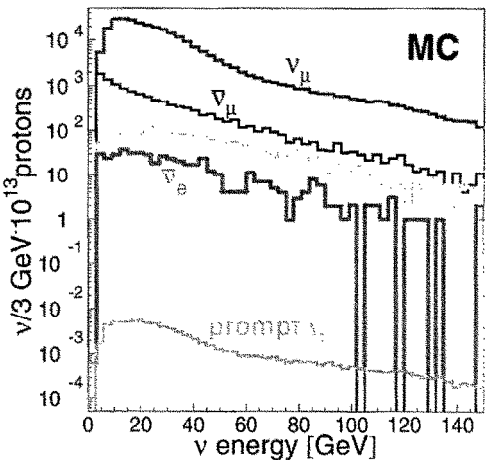

Fig. 6. Energy spectra of the different neutrino components in the WBB at the location of the CHORUS emulsion target (transverse dimensions $1.44 \times 1.44\,m^2$), as derived from the neutrino beam simulations.

4. The emulsion target and the interface sheets

The emulsion set-up consists of two components: (a) the emulsion target, where neutrino interactions are recorded, and where the typical decay topologies are searched for among the trajectories of the charged particles from the vertices; and (b) the thin emulsion sheets, which are used as a high-accuracy interface between fiber trackers and target. Depicted in Fig. 7 is the principal arrangement of the target region, showing the emulsion target and interface sheets (labelled "CS" and "SS"), with the target tracker modules. The complete target region is made up of two such arrangements, one behind the other.

The emulsion target has a total volume of 206 l for a mass of 770 kg. As the total thickness of the target amounts to almost 4 radiation lengths ($X_0 \sim 29$ mm in emulsion) and 0.32 interaction length (one interaction length corresponds to 35 cm of emulsion), it is divided into four stacks each having a surface area of $1.42 \times 1.44\,m^2$ and a thickness of 2.8 cm. Each stack is further subdivided into 8 sectors of $0.71 \times 0.36\,m^2$ area, each consisting of 36 emulsion sheets. In each plate, emulsion gel [17] with a thickness of 350 μm is poured onto both faces of a 90 μm thick tri-acetate cellulose foil. Each face is dried for 2 days at 20°C and a relative humidity of 80%. The plates are subsequently piled-up in close contact within one sector and vacuum packed within a thin shielding envelope

[17] The emulsion gel used is the ET-7B produced by Fuji, Japan, and BR-2M produced by NII KHIMFOTO PROEKT PLC, Russia.

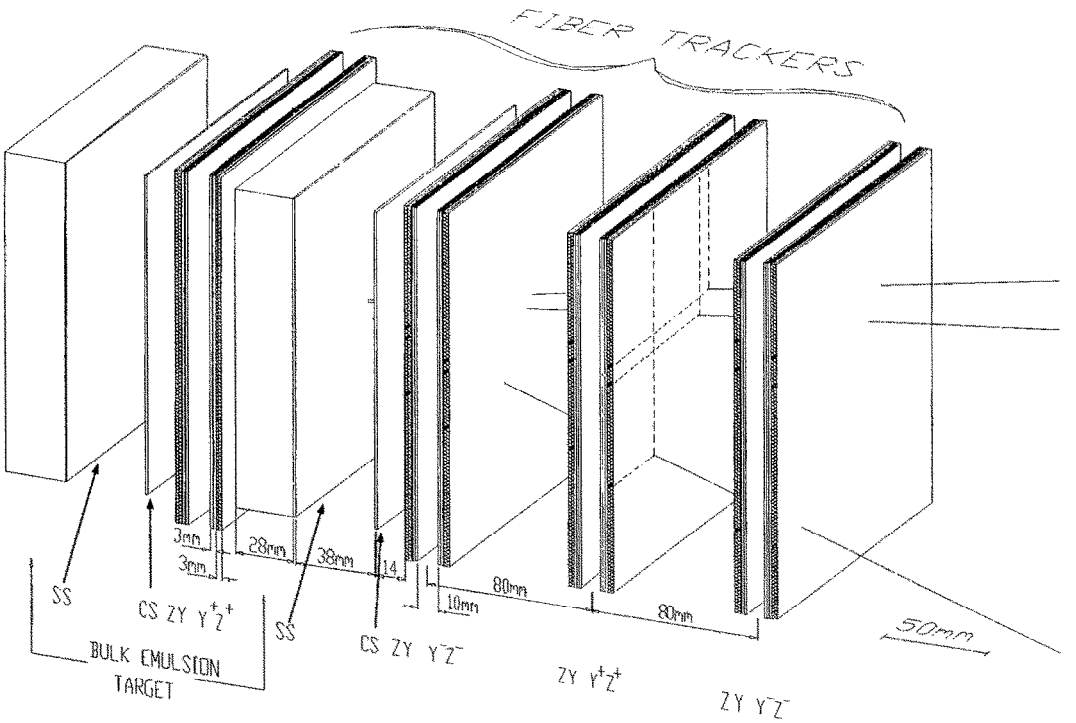

Fig. 7. The geometry of the target region, showing the target emulsion target stacks and the interface sheets (CS and SS), with the target trackers. The labels Y, Z, $Y^{\pm}$, $Z^{\pm}$ denote the different orientations of the target tracker planes. The complete target region consists of two such arrangements. Further details on the geometry of the interface sheets and the emulsion target are shown in Fig. 2.

made of aluminized paper, to preserve their initial water content.

Downstream of each emulsion stack are three sets of interface emulsion sheets with the same lateral dimensions, each consisting of an acrylic plate 0.8 mm thick coated on both sides with a 100 μm thick emulsion layer. They are placed between the emulsion target and the next downstream fiber tracker module, as shown in Fig. 7. The "special sheet" (SS) is packed at the downstream side of the target emulsion stack, and is replaced by a new sheet after one year of exposure. The two "changeable sheets" (CS1 and CS2) are mounted at the two faces of a 1 cm thick honeycomb panel, positioned in front of the first fiber tracker module downstream of the emulsion target. In the 1994–1995 data taking, the changeable sheets were replaced every three to six weeks during the running time of the experiment, to provide favourable background conditions for the recognition of the predicted tracks in the emulsion. In the 1996–1997 data taking only one change per year was found necessary, due to the reduction of the background.

The relative alignment among the interface sheets (both CS2 to CS1 and CS1 to SS) is realized by means of sets of 15 X-ray "guns" per sector, that produce a pattern of black dots ("fiducial marks") of 1 mm diameter in each pair of sheets. The X-ray guns (brass cylinders filled with ^{55}Fe sources) are placed in a honeycomb structure that also keeps the desired distance between sheets. The relative alignment between adjacent emulsion layers is realized by the tracks of passing-through muons.

The combination of fiber trackers and emulsion sheets provides the needed time resolution in correlating tracks of particles from selected events, while keeping the desired high spatial resolution. In order to handle high-multiplicity events, the first planes of

the fiber trackers are placed 50 mm downstream of the emulsion target. The changeable sheet CS1 is at a distance of about 1 mm (15 mm for CS2) to the closest fiber plane to reduce extrapolation errors.

The target emulsion stacks are positioned vertically inside a rigid frame with the changeable sheets and the scintillating fiber trackers. Particles originating from neutrino interactions are emitted at small angles with respect to the beam, so that tracks are almost perpendicular to the emulsion plates. This allows fast semi-automatic [12] and automatic scanning [13] to be performed.

Each set of target emulsion is used for two years of data taking in the neutrino beam. The total exposure time in the beam is about 10 months. Special care is required to keep under control the process of emulsion fading (the erasing of the latent image due to diffusion, which is strongly dependent on the temperature) and the accumulation of background tracks (which reduces the visibility in emulsion scanning). To reduce fading, the emulsion stacks are kept at a temperature of $(5.0 \pm 0.5)^{\circ}$C in a cool box containing the whole target area, the hexagonal magnet, the associated fiber trackers and the trigger planes, as shown in Fig. 3. As a result, the change in the lateral dimensions of the emulsion due to thermal variations is also minimized. The relative humidity of the cool box is stablized at 60%.

Possible background sources are systematically monitored and shielded. The number of cosmic ray tracks, that sum up to $180\,\mathrm{m}^{-2}\,\mathrm{s}^{-1}$ on a horizontal surface, is halved by always keeping the undeveloped emulsion plates vertical, since the flux strongly peaks around the vertical axis. Although these tracks have completely different directions, and can hardly simulate those from a neutrino interaction, they can pile-up to a dangerous level over long periods. Therefore, during the six months shutdown between the exposures of two consecutive years, the emulsions are stored inside a cooled iron shield 150 m underground (in the LEP-ALEPH pit), so that the cosmic-ray flux is reduced to less than 0.1%. The ambient radioactivity at the CHORUS location, mainly consisting of low-energy gamma rays originating from the concrete of the floor and of the walls, and giving rise to short-range Compton or photo-electrons in emulsion, is efficiently shielded by inserting 8 cm thick iron plates around the target.

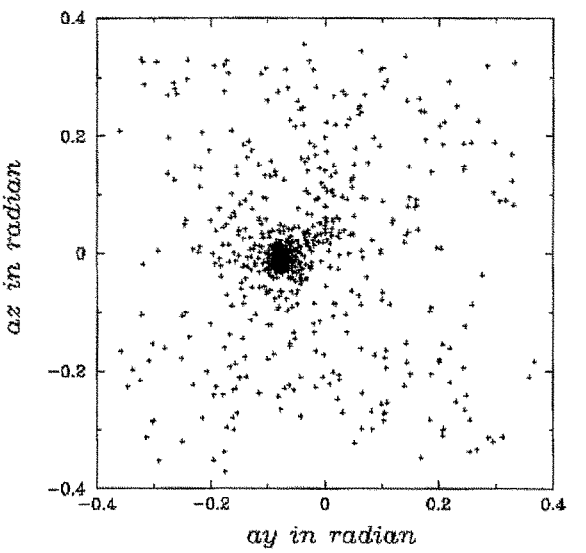

Fig. 8. Angular distribution of muons in the emulsions. The peak corresponds to the "X7" test beam direction, and αy and αz denote angles relative to the horizontal and vertical axes of the CHORUS detector planes, respectively.

There is also background, predominantly penetrating muons, arising from secondary SPS West Area beams. The major source is a test beam ("X7") also used by CHORUS for calibration purposes (see Section 12). Fig. 8 shows the angular distribution of emulsion tracks during a typical run: the dominance of the muons associated with the X7 beam is conspicuous. The flux of these muons is reduced by imposing constraints on the beam polarity, intensity and energy. As an example, the X7 beam, tuned for 100 GeV/c negative particles, produces at the target position a flux of muons about 10 times larger than other sources, and about 5 times larger than when it is set at 30 GeV/c or for positive particles. Therefore, X7 is only allowed to run with positive polarity during the neutrino exposures, at a typical momentum of 25 GeV/c. The muons originating from X7 are out-of-time with respect to the neutrino spill, and hence do not contribute to any trigger. In the emulsion scanning an angular cut around the direction of the X7 muons is applied to minimize contamination to the neutrino-event related tracks. However, since the X7 muons are recorded in the emulsion, they are used for the internal alignment of emulsion sheets and for distortion corrections.

5. The fiber tracker and optoelectronic read-out system

5.1. Scintillating fiber tracker

Scintillating fibers are adopted to provide tracking downstream of the emulsion target because of their good spatial and two-track resolution. The choice of optoelectronic read-out allows a cost-effective system to be built. The CHORUS fiber tracker system [14] is based on a total of more than one million plastic scintillating fibers[18] of 500 μm in diameter and 2.3 m in length (comprising 1.6 m of useful detector element and 0.7 m of flexible light guide). Fiber ribbons with 7 layers in a "staggered" geometry were constructed using a specially designed fiber-winding machine [15]. Each layer is painted with a TiO_2-based white paint, which acts both as a glue and as an extra-mural absorber (EMA) to prevent cross-talk. The far ends of the ribbons are polished and sputtered with aluminium. The reflectivity thus obtained is about 80%. The tracker system consists of two components:

The target tracker (TT): The target region consists of four target emulsion stacks and eight target tracker modules, half of which are shown schematically in Fig. 7. Each tracker module consists of four projection planes (Y, Z, and $Y^{\pm}$ $Z^{\pm}$ rotated by $\pm 8°$ relative to Y, Z). Each projection plane is constructed with 7-layer ribbons. There are 8 target tracker modules altogether, interleaved between the 4 target emulsion stacks, as depicted in Fig. 7. By using the information from the four projections, three-dimensional trajectories of traversing particles can be unambiguously reconstructed.

The major role of the target tracker is to locate the stack where the neutrino interaction takes place, and to make accurate track predictions at the interface emulsion sheets (shown as CS in Fig. 7). Both informations are essential for track scanning and following back into the emulsion target. The distance between the target emulsion stacks and the closest downstream tracker module (40 mm) is defined by two conflicting requirements: the two-track separation at the tracker and the accuracy of the track prediction extrapolated back.

[18] SCSF-38, Kuraray, Japan.

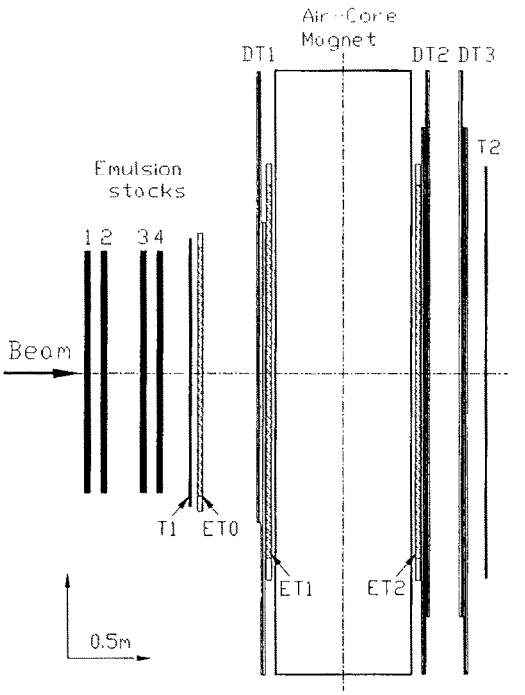

Fig. 9. Geometry of the magnet trackers (DT) and the emulsion trackers (ET) around the air-core magnet.

The "diamond-shaped" magnet tracker (DT): As displayed in Fig. 9, there are three magnet tracker modules, one upstream and two downstream of the air-core toroidal magnet. Each tracker module has hexagonal shape and consists of two planes. Three adjacent "paddles", arranged as shown in Fig. 10, constitute one plane, which allows to measure the three coordinates at 120° from each other. The second plane is rotated by 60° with respect to the first, providing measurement of the complementary coordinates. Paddles are made up of 7-layer ribbons. Both the magnet and the tracker have the same six-fold symmetry, such that one of the two coordinates measured by each module is in the bending plane. The magnet tracker measures the charge and momentum of the particles (in particular, of the daughters from the decay of the τ) originating from a neutrino interaction at the target.

5.2. Optoelectronic read-out system

The optoelectronic technology allows a cost-effective read-out system to be built for the one

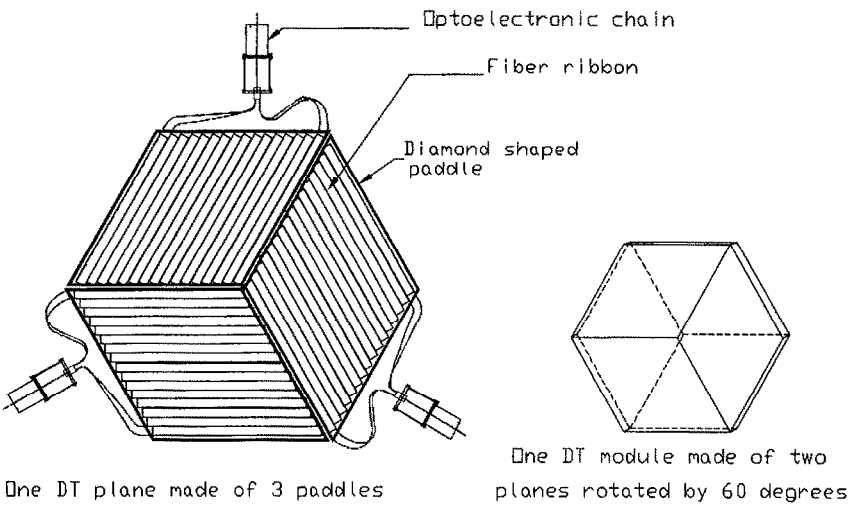

Fig. 10. Schematic layout of one module of the magnet ("diamond") tracker, showing the orientations of the six paddles.

million fibers. At the read-out ends, the fiber ribbons are bundled together and coupled to a total of 58 optoelectronic read-out chains, each of them consisting of four image intensifiers and a CCD camera[19] [16], as depicted schematically in Fig. 11.

A medium-slow phosphor P11 with 50 (90)% of the light collected in 50 (500) μs is adopted for the first image intensifier stage (an elctrostatic demagnifier from 100 to 25 mm) so that only a negligible amount of light is lost in the first 0.5 μs due to trigger delay. The phosphor chosen for all other stages is the fast P46. The photocathode of each stage is optimized to match the spectral emission of the preceeding stage. Background considerations restrict the integration time of the gateable Micro-Channel Plate (MCP) to be 20 μs or less, corresponding to the collection of about one third of the light emitted by the first stage. The net gain of the entire assembly of the image intensifiers ranges from 10^4 to 10^5, and the net demagnification factor from the fiber bundle input to the CCD surface is 0.11.

The CCD sensor contains an image zone and a memory zone, with an "antiblooming" facility in the image zone to provide fast clear capabilities in 1 μs. The antiblooming consists of a special electrode-grid placed between pixel rows and columns. It prevents charge to flow from one pixel to the neighbouring ones.

Each zone consists of 550×288 pixels with $16 \times 23\ \mu m^2$ dimensions, corresponding to $145 \times 209\ \mu m^2$ in the detector space. The transfer time from the image to the memory zone is about 125 μs, while the read-out of one image, done during the interspill or interburst intervals, takes 20 ms per event. Therefore, the system can record two events in the neutrino spill which lasts for 6 ms.

The schematic diagram of the CCD read-out and data acquisition is shown in Fig. 12. The CCD camera design is based on a central generation of trigger and synchronization signals that are further distributed to the individual CCD sensors. The 8-bit digitized data from each sensor are combined together with the video synchronization signals by specially designed translator cards. The resulting data are subsequently transferred via a video interface bus to a VME image processor board[20] [16]. A total of 29 processor modules are required to read-out the 58 image intensifier and CCD chains. They perform on-line data processing and compression during interspill time and

[19] (100/25) electrostatic image intensifier – Hamamatsu Photonics, Japan; (25/25) and (25/11) electrostatic image intensifiers – Delft Electronische Produkten (DEP), The Netherlands; (25/25) MCP – Proxitronic Funk, GmbH & Co., Germany; CCD sensor – Thomson TH7864, Thomson, France.

[20] VME SL30 processor – Eltec, Mainz, Germany.

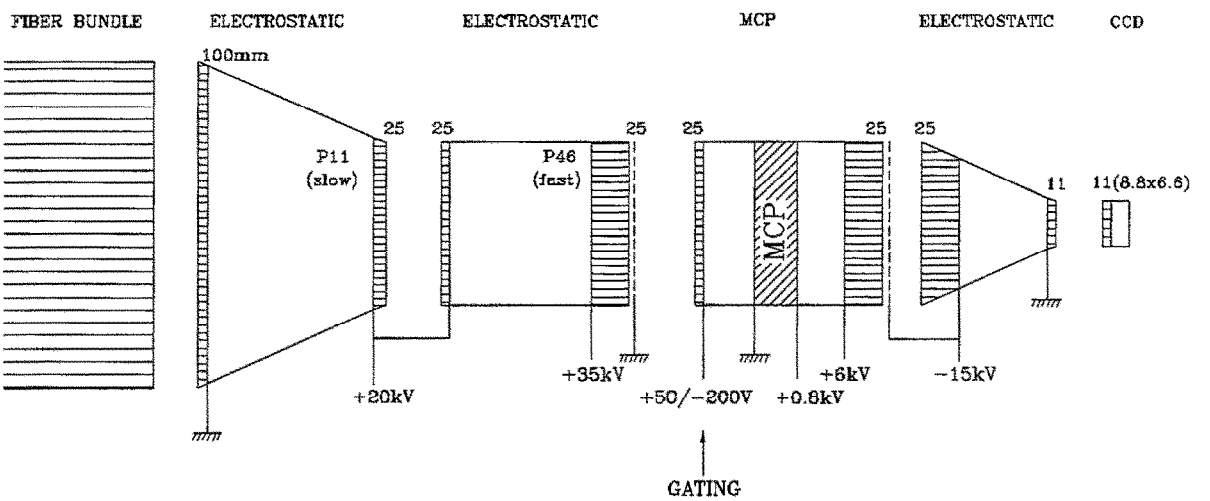

Fig. 11. The optoelectronic read-out chain.

typically require 1 s per event. The compressed data are then transferred to the central CHORUS data acquisition system.

In order to measure the image distortion and to monitor the performance of the optoelectronic read-out, a calibration system (shown schematically in Fig. 13) was constructed [16]. A set of 45 "fiducial" fibers, each with 127 μm diameter, is coupled to an optoelectronic chain with light input supplied by a computer-controlled LED pulser. Based on measurements with the fiducial calibration system, the performance of the optoelectronic read-out can be monitored independently of the fiber trackers.

5.3. *Intrinsic hardware performance*

The average quantum efficiency of the optoelectronic chains was determined to be 18%, from measurements performed using a photomultiplier with known quantum efficiency. By comparing the given positions of the fiducial fibers at the input window with the measured ones on the CCD, a distortion correction can be evaluated. The achieved accuracy corresponds to a resolution (at the fiber tracker level) of $\sigma \sim 110\,\mu$m, transverse to the beam axis.

Two parameters characterize the spatial resolution of the read-out system. The "spot size" (the width of the charge distribution induced on the CCD from a single photoelectron in the first image intensifier) is due to the intrinsic resolution of the optoelectronic read-out chain. The "spot displacement" (the deviation of the center of gravity of a cluster from its mean position) is caused mainly by the focusing of the first image intensifier. Based on measurements with the fiducial fibers, the standard deviation for the spot size and displacement at the input window are 136 and 89 μm, respectively.

Muons associated with the neutrino beam provide minimum-ionizing particles for the measurement of the intrinsic properties of scintillating fibers. The signals recorded by the CCD when such muons traverse a fiber ribbon are shown in Fig. 14. The ribbon hit density as a function of the distance from the read-out is shown in Fig. 15. The measured hit density is about 5 and 7 hits/ribbon at the far (220 cm) and near (70 cm) ends of the detector, respectively. The "bare fiber" light attenuation length is about 220 cm, while the "effective" attenuation length of the tracker system (fibers with mirrored ends) is about 600 cm. No observable deterioration of the attenuation length (fiber ageing effect) over the course of 30 months was detected. The tracker detector inefficiency per ribbon (the probability for a minimum-ionizing particle to pass without producing any signal recorded by the CCD) is evaluated using beam muon data, and amounts to 2×10^{-3}.

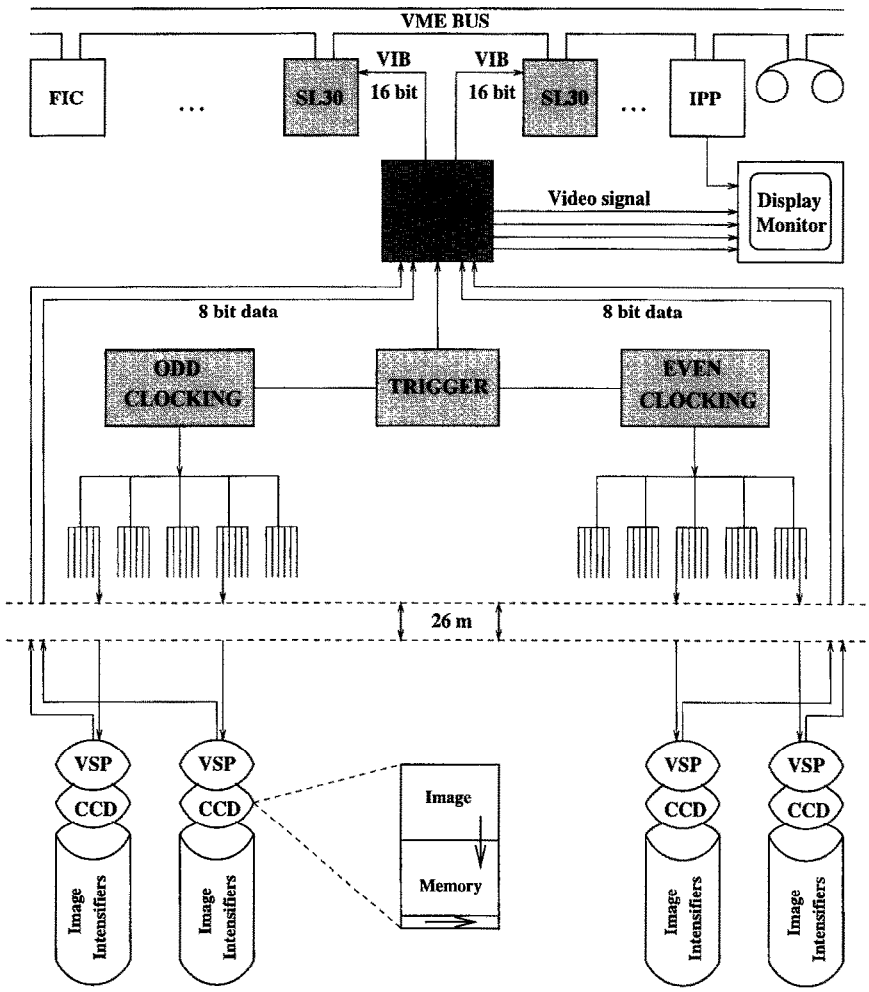

Fig. 12. The CCD read-out and the data acquisition system.

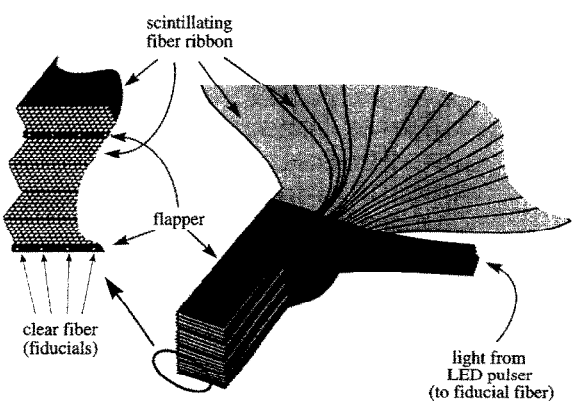

Fig. 13. View of the fiducial fiber calibration system.

Muons associated with the neutrino beam, as well as cosmic ray muons, are used to align the different planes of the fiber trackers with a resulting accuracy of 20 μm for each degree of freedom. After the alignment procedure is performed, the measured track residual per fiber ribbon has a width $\sigma \sim 180\,\mu m$.

Based on measurements of several hundred of beam muons located at the interface emulsion sheets, the prediction accuracy for isolated minimum-ionizing tracks (deviation of the target tracker predictions on the emulsion sheets from the found tracks) is $\sigma \sim 150\,\mu m$ in position and ~ 2.5 mrad in angle. By unfolding the expected intrinsic resolution of 1.5 mrad for the emulsion sheets, the

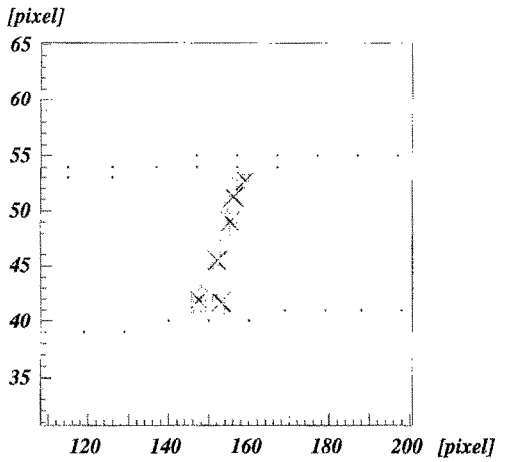

Fig. 14. Typical signatures of a muon traversing a fiber ribbon, as recorded by the CCD. The units are in CCD pixel, translating to $X = 145\,\mu m$ and $Y = 209\,\mu m$ per unit in detector space. The shading of the pixels (gray and black) denotes their pulse height. Superimposed as crosses are identified "hits". Small black dots denote the ribbon boundary as parametrized from contact print pictures.

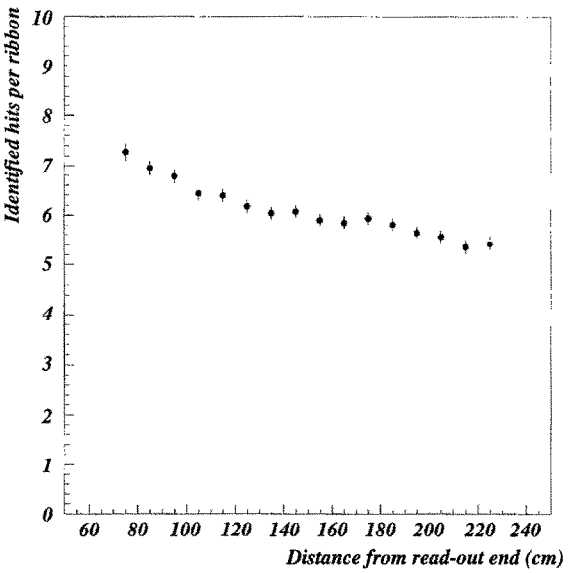

Fig. 15. Measured hit density per fiber plane as a function of the distance from the read-out end. The light yield of 5–7 hits per plane over the active surface ensures high detection efficiency.

intrinsic angular resolution of the fiber tracker alone is $\sigma \sim 2$ mrad.

6. The hexagonal magnet

An air-core magnet of hexagonal shape is located between the target region and the calorimeter for the measurement of the charge and momentum of particles before they enter the calorimeter. The momentum measurement is also used to predict the range of low energy (1–2 GeV/c) muons which do not reach the muon spectrometer. The air-core magnet is installed as an integral part of the target region in the cool box, which provides a constant ambient temperature of 5°C.

Severe constraints were imposed on the magnet design. A stray field would prohibit the use of electrostatic image intensifiers for the fiber trackers, and complicate the tracking unnecessarily. The magnet length is restricted in order not to reduce the acceptance of the downstream calorimeter and spectrometer. The amount of material traversed by particles needs to be minimized.

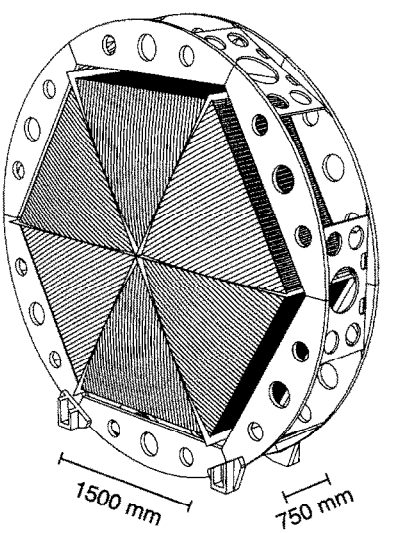

Fig. 16. Drawing of the hexagonal magnet.

The toroidal air-core magnet was built to satisfy these constraints. It is made of six equilateral triangles with 1.5 m sides, 0.75 m depth, and housed in a cylinder with 3.6 m diameter, as shown in Fig. 16.

Windings of thin aluminium sheets cover all faces of the triangles, producing in each triangle section a homogeneous field parallel to the outer side. The field strength has no radial dependence.

The material of the front and back faces corresponds each to less than 4% of a radiation length. The six spokes of the magnet, formed by two sides of adjacent triangles, represent a dead space for momentum reconstruction. Averaged over all charged tracks with momentum between 2.5 and 10 GeV/c the geometrical acceptance of the magnet is 85%. The magnet current is pulsed with a duty-factor of $\sim 4 \times 10^{-3}$, to follow the time structure of the neutrino beam. A field of 0.12 Tesla is obtained with a power dissipation of 15 kW. The stray field is ~ 1.5 Gauss at 1 cm distance from the magnet surface. The dense packing of detectors in front and behind the magnet requires this heat to be dissipated by blowing cold air along the conductors at the inside of each magnet triangle. The warmed-up air is then collected and evacuated to the outside of the cool box. More details on the magnet design and construction can be found in Ref. [17].

The momentum resolution $\Delta p/p$ of the magnet tracker results from the quadratic combination of two terms: a constant term, evaluated at 22%, from the multiple scattering in the traversed material (mainly the front and exit faces of the magnet) and a term proportional to the momentum, which reflects the measurement accuracy. The value expected for this term from the intrinsic tracker resolution is $(\Delta p/p)_{\text{expect}} = 2.5\% \times p\,\text{GeV}/c$.

Beam muon data were recorded with the air-core magnet being pulsed. By comparing to the momentum measured by the muon spectrometer system, the resolution of the magnet trackers can be evaluated. Displayed in Fig. 17 are the RMS values of the relative difference between the measurements by the spectrometer and by the magnet tracker as a function of the spectrometer momentum. This distribution is well reproduced by convoluting the known spectrometer resolution ($\Delta p/p \sim 7\%$ below 6 GeV/c, where the range of the stopping muon is used, and $\sim 16.5\%$ above 6 GeV/c, where the curvature is measured) and a tracker resolution giving rise to a $(\Delta p/p)_{\text{meas}} = 3.5\% \times p\,\text{GeV}/c$, as indicated by the solid line in Fig. 17. The sign of the charge for particles with momentum of 5 GeV/c can then be determined with better than the three standard deviation

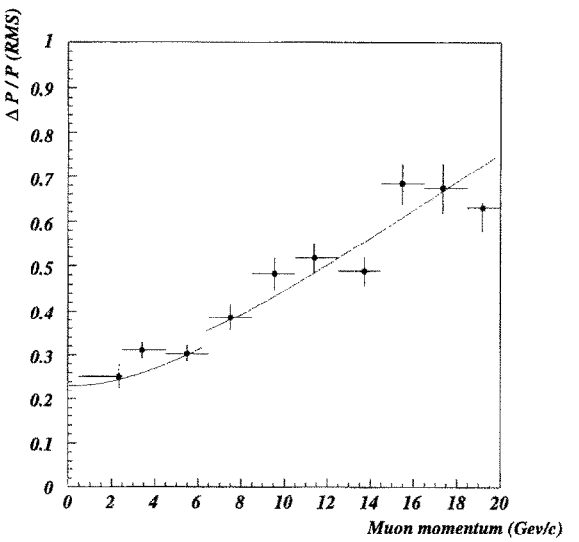

Fig. 17. Momentum resolution for particles traversing the hexagonal magnet, as measured by the magnet trackers (preliminary).

level. Residual alignment problems such as imperfect planarity and thermal effects caused by the magnet pulsing are currently being investigated as possible sources of this discrepancy from the design resolution.

7. The calorimeter

The electronic detectors provide measurements of the kinematical variables crucial for: (a) the selection of events for emulsion scanning, and (b) the suppression of background events with the typical decay topologies. Both tasks require that the hadron shower from the neutrino interaction is measured with good angular and energy resolution by a calorimeter. In order to detect the muonic decay of the τ, it is also necessary to efficiently track throughgoing muons in the calorimeter and to match their trajectories with those determined by the other detectors of the apparatus.

The CHORUS calorimeter was designed to fulfill these requirements. It is the first large scale application of the calorimetric technique of embedding scintillating fibers into a lead matrix [18] (the "spaghetti" technique). Scintillating fibers of 1 mm diameter and lead as passive material, with a lead to scintillator volume ratio of 4 : 1, were chosen to assure both compensation and good sampling, and consequently good

hadronic energy resolution. The fibers are placed in a direction perpendicular to the beam direction, to provide angular measurements of the showers as well as tracking of muons. Such a transverse configuration allows for the insertion of streamer tube chambers to provide tracking capabilities and it also reduces the effect of light attenuation. The most downstream part of the calorimeter is a lead/scintillator-strip sandwich with the same volume ratio of 4 : 1.

7.1. The calorimeter design

The calorimeter has a modular construction, in which the elements are arranged to form planes perpendicular to the beam and alternating in the horizontal and vertical direction. The width of the modules is chosen to be much smaller than the size of the average hadron shower, in order to reconstruct the center of gravity of the energy deposited by the hadrons produced in the interactions with good accuracy. The calorimeter consists of three sections with decreasing granularity, called EM, HAD1 and HAD2. The first section measures the electromagnetic component of the hadronic shower in neutrino induced events, while the other two sections complete the measurement of the hadronic component. The total depth corresponds to 144 radiation lengths and 5.2 interaction lengths. Consequently, 99% of the showers produced by a 5 GeV/c pion can be contained (about 90% of the hadrons produced in neutrino interactions have momentum less than 5 GeV/c). EM and HAD1 are made of scintillating fibers and lead, while HAD2 is made as a sandwich of lead and scintillating strips.

Between the horizontal and the vertical planes of calorimeter modules, 22 planes of streamer tube chambers are inserted to allow tracking of the penetrating charged particles, with digital signals recorded from the wires. Details of the streamer tube chambers, which are also used in the muon spectrometer, are described in Section 8.3.

The calorimeter is shown in Fig. 18. A detailed description of the module construction and test can be found elsewhere [19]. Only the main features are summarized here.

Two horizontal and two vertical planes, each of 31 modules, make up the EM section. Individual modules are built by piling-up extruded layers of grooved lead and plastic scintillating fibers positioned in the grooves. The groove diameter is 1.1 mm and the layer thickness 1.9 mm; the material, the same as for the HAD1 and HAD2 modules, is lead and 1% admixture of antimony, to improve the mechanical properties. A module consists of a pile of 21 layers, 2620 mm long and 82.4 mm wide, and 740 fibers of 3050 mm length. On either side of the module, fibers are assembled in two hexagonal bundles, defining two different read-out cells with about $40 \times 40\,\mathrm{mm}^2$ cross-section. Each of the fiber bundles is coupled to a 1″ photomultiplier (PM) via a plexiglas light guide.

The HAD1 section consists of 5 planes (three horizontal and two vertical). A plane is formed by 40 modules, each made of 43 extruded layers of lead identical in width and groove size to those used for the EM section, but with a length of 3350 mm. The scintillating fibers have 3810 mm length, for a total of 1554 fibers per module. Fibers are collected at both ends in a hexagonal bundle coupled via a light guide to a 2″ PM.

The HAD2 section consists of 5 planes (three vertical and two horizontal) with 18 modules each, making a total of 90 modules. Each module is constructed by having five alternate layers of lead bar ($3690 \times 200 \times 16\,\mathrm{mm}^3$) interleaved with two adjacent scintillator strips ($3714 \times 100 \times 4\,\mathrm{mm}^3$ each). It is packed into a stainless steel box open at both ends. Each of the two groups of five scintillators is coupled to 2″ PMs at both ends via plexiglas light guides; therefore, a single module is seen by a total of four PM tubes, and contains two cells.

The analog signal of the 1256 photomultipliers of the calorimeter is digitized by dual-range 8-bit ADCs. The nominal ratio of the conversion factors for the two ADCs (high/low sensitivity) is set to 20 for all the channels: the actual value of this ratio for each ADC is determined and monitored experimentally by means of cosmic ray events. The ADC integration gate is 220 ns wide.

7.2. Test beam performance

The intrinsic performance of the calorimeter was determined in several measurements with test beams of well-defined energy, performed on single modules and on the completely assembled detector. In the latter case, the calorimeter, mounted on rails, was shifted sideways with respect to its location in CHORUS to

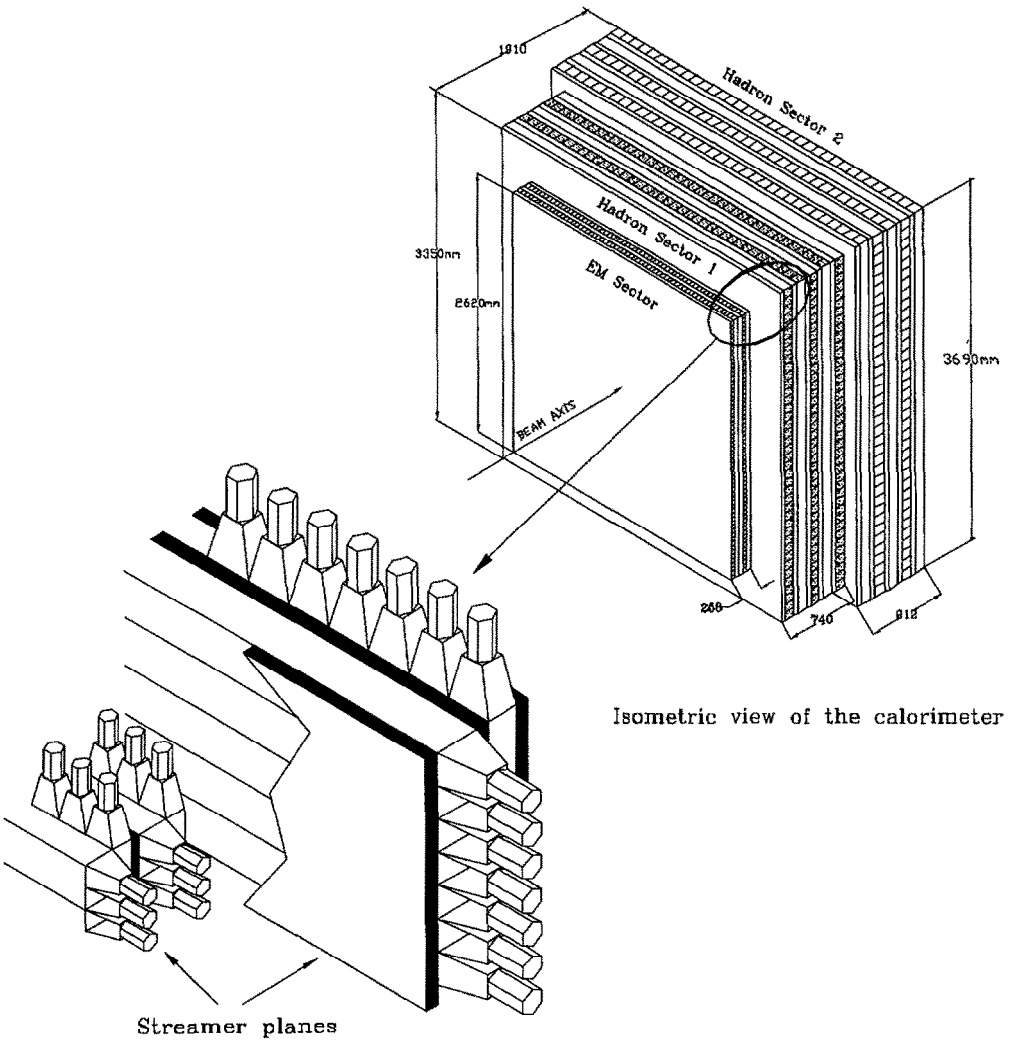

Fig. 18. Schematic view of the calorimeter.

meet a SPS X7 test beam [20]. Another branch of this beam, the so called "direct beam", is pointing to the target region, nearly collinear to the neutrino beam (see Section 12).

The electron response was studied for different beam momenta in the range from 2.5 to 10 GeV/c, relevant for the CHORUS experiment. For each momentum, a Gaussian fit is performed to the distribution of the calorimeter signal, which is the calibrated sum of the response of all modules, as obtained by computing the geometric mean of the two photomultiplier signals of each module (see Section 12). The energy resolution $\sigma(E)/E$, is plotted in Fig. 19 as a function of the electron energy. The energy dependence is well fitted by the function:

$$\frac{\sigma(E)}{E} = \frac{(13.8 \pm 0.9)\%}{\sqrt{E(\mathrm{GeV})}} + (-0.2 \pm 0.4)\%.$$

This result agrees with the Monte Carlo predictions. By studying electron showers developing in different calorimeter zones, we estimated the nonuniformity in the electromagnetic response to be of the order of $\pm 5\%$.

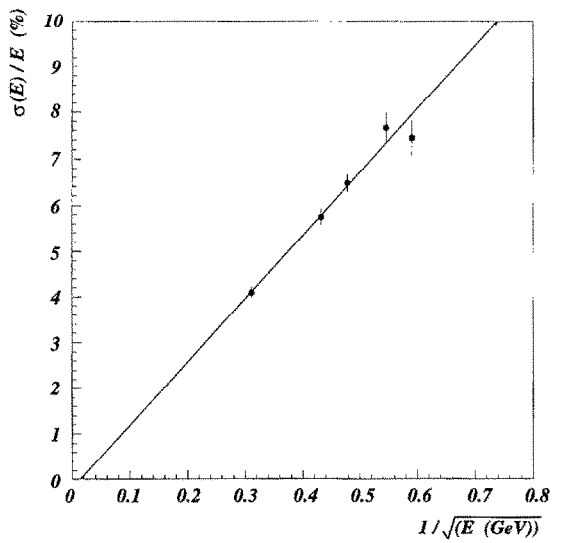

Fig. 19. The electromagnetic energy resolution of the calorimeter.

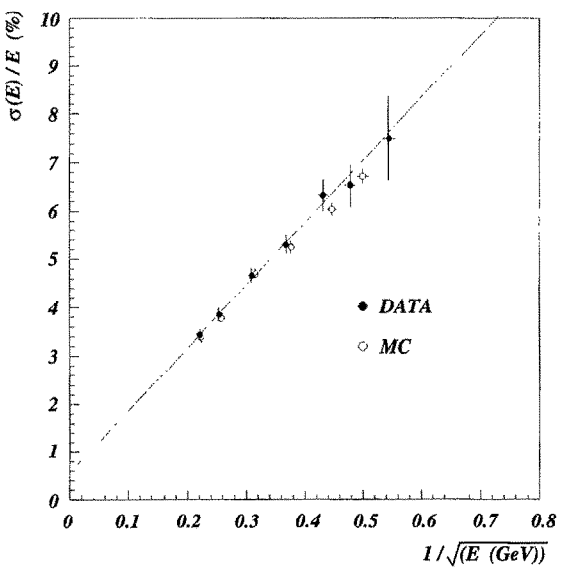

Fig. 20. The hadronic energy resolution of the calorimeter.

The response to pions was studied in the range from 3 to 20 GeV/c. The measured pion momentum dependence is found to be linear up to the highest energy within less than 2%. From a Gaussian fit to the response distributions one determines the energy resolution $\sigma(E)/E$, which is plotted in Fig. 20 as a function of the pion energy. The errors assigned to each point include a systematic uncertainty of about 2%, evaluated by applying different event selection criteria to the data, and by studying pions hitting different calorimeter positions. The above uncertainty is lower than in the electron case (±5%). The main reason is the larger number of calorimeter modules involved in a hadron shower. The energy dependence of the hadronic resolution is parametrized as:

$$\frac{\sigma(E)}{E} = \frac{(32.3 \pm 2.4)\%}{\sqrt{E(\mathrm{GeV})}} + (1.4 \pm 0.7)\%.$$

The predictions of a Monte Carlo simulation, also shown in Fig. 20, are consistent with the data. Further results on the performance of the calorimeter may be found in Ref. [21].

8. The muon spectrometer

The role of the CHORUS muon spectrometer[21] is to identify muons and determine their trajectory, momentum and charge. The spectrometer is located behind the calorimeter whose 5.2 hadronic interaction lengths filter nearly all the particles produced by neutrino interactions in the emulsion target except muons with momentum higher than ~1.5 GeV/c. As displayed in Fig. 21, the spectrometer is constructed from six magnetized iron toroid modules and tracking detectors consisting of drift chambers and limited streamer tubes. In addition, scintillator planes interleaved with the magnet iron provide a measurement of the leakage of hadronic showers from the back of the calorimeter. The fast signals from these scintillator planes are also used for triggering.

The momentum resolution of the muon spectrometer is about 19% at 71 GeV/c, as measured with test beam muons (Section 12.3). At lower momenta it is determined with the help of a Monte Carlo simulation and the results are shown in Fig. 22.

8.1. Magnets

The momentum of a muon is determined from the change of its trajectory in the six toroidal magnets,

[21] The magnet modules and the drift chambers were kindly lent by the CERN CDHSW Collaboration.

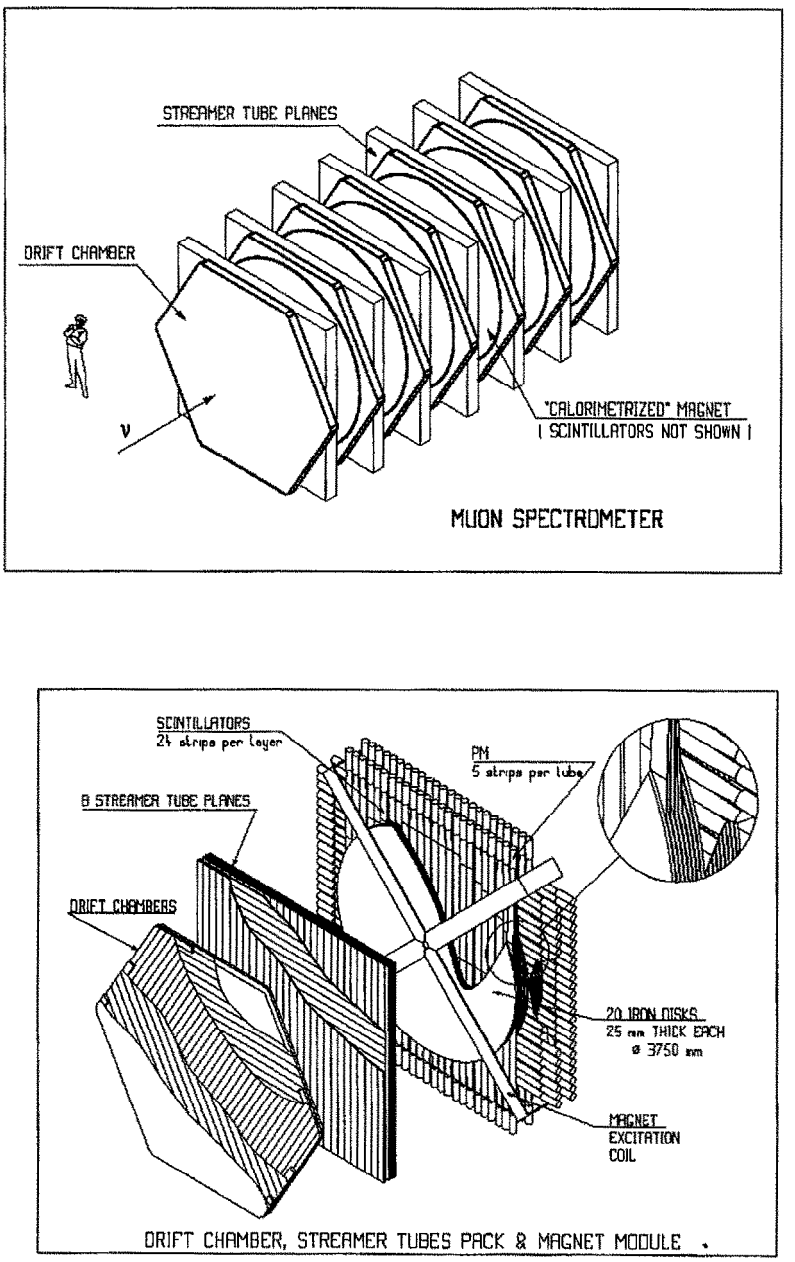

Fig. 21. Muon spectrometer with details of the tracking and of the scintillator hodoscope.

originally used as calorimeter modules in the upgraded CDHS detector [22] and later in the CHARM II end-system [23]. Each magnet is constructed from twenty 2.5 cm thick iron disks with an outer diameter of 375 cm, interleaved with 0.5 cm thick scintillator planes inserted into 0.6 cm gaps between the disks. Each magnet weighs about 43 tons.

The iron is magnetized by four water-cooled copper coils passing through a 8.5 cm wide hole in the center of each magnet. The field in iron is nearly

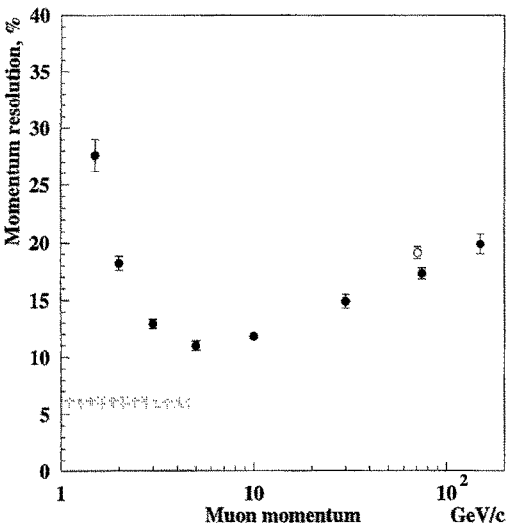

Fig. 22. The muon spectrometer momentum resolution as function of incident momentum. Full dots: Monte Carlo events, the open dot at 71 GeV/c: test beam muons. The shaded band corresponds to muons stopping in the spectrometer, with their momentum determined by range.

symmetric in azimuthal angle and varies by 25% along the radius, providing a field integral of approximately 0.85 Tesla m per magnet [22]. To maximize the acceptance for τ^- decays, the polarity of the current of 700 A is set such that negatively charged muons are focused, i.e. bent towards the center of the magnets. The magnets are separated by 120.8 cm along the beam and placed vertically. The centers of the magnets are positioned so they follow the 42 mrad slope of the beamline.

8.2. Drift chambers

The seven drift chambers [24] are part of the original detector used by the CDHS experiment, and provide tracking in the muon spectrometer. They are mounted vertically, one chamber in each of the seven tracking gaps in front of or behind the six magnets, and placed so that their centers follow the slope of the neutrino beam. Each chamber consists of three hexagonal drift planes oriented at 60° with respect to each other, with the wires of the rear plane oriented horizontally. Each plane has 62 parallel sense wires (40 μm diameter, 375 cm long) separated by 6 cm and interleaved with cathode wires.

The chambers are filled with 60% argon −40% ethane mixture. The anode sense wires and the cathode wires are held at a potential of 3700 V and −1000 V, respectively. An approximately uniform electric field along the 3 cm drift path is obtained by another row of field correction wires. The drift velocity is 5.3 cm/μs. Signals are amplified by chamber-mounted preamplifiers and then read-out by TDCs with 10 ns resolution, operating in "common-stop" mode. These TDCs can record up to 4 hits per event, sufficient to handle neutrino data since typically only one track (the muon) is recorded in the spectrometer. The signals are distributed in such a way that any four consecutive wires are read-out by different TDC units.

The hit resolution of the drift chambers is about 1 mm and the efficiency per plane better than 99%. With the chamber alone, right–left ambiguities can be resolved for 83% of forward going tracks.

8.3. Streamer tube chambers

Each of the seven drift chambers is followed by a stack of eight limited streamer tube planes of the former CHARM II calorimeter [23], slightly modified to reduce wire cross-talk effects. They provide measurement of track segments in each gap and eliminate unresolvable right–left ambiguities in the corresponding drift chamber.

Each plane, covering an active area of $367 \times 367\,\mathrm{cm}^2$, consists of 352 square-shaped limited streamer tubes with the inner area of $9 \times 9\,\mathrm{mm}^2$ and an average wire spacing of 1.05 cm. The tubes are operated with a 27% argon−73% isobutane mixture, plus a 0.4% admixture of water vapour to prevent organic deposits on the wires. A positive high voltage of 4300 V is applied to a conductive graphite coating of the inner walls of the PVC tubes. The anode wires are held at ground potential and coupled directly to the electronics.

External to the streamer tubes are 18 mm wide cathode pick-up strips with 21 mm spacing, orthogonal to the wire direction. They measure the track position along the wire, identified by the center of gravity of the induced charge distribution. Consecutive planes have alternating horizontal and vertical wire orientations, so that each stack of streamer tubes in a tracking gap provides up to eight independent coordinate measurements in each of the two views. On average,

a forward going muon produces 3.6 wire hits and 3.2 usable strip hits per view in a gap.

The original CHARM II electronics have been upgraded to supplement the digital tube read-out with drift-time measurement. The drift velocity saturates at $\sim$5 cm/μs, and a linear space-time relationship is assumed. The maximum drift-time is 90 ns for normal incidence tracks.

The signals from each group of 8 consecutive wires are combined to form 44 drift-time read-out cells per plane. Since the occupancy of the muon spectrometer is low, the digital hit pattern can be used to uniquely identify the wire in a cell. There are fewer than 0.1% persistently inactive wire channels and the hit efficiency per plane for beam muons is (90 ± 2)%, consistent with the geometrical acceptance.

Signals from four consecutive cells are multiplexed to a single input of a 10 ns TDC of the same type as used for the drift chambers. The multiplexing is achieved by delaying the four signals by about 300 ns with respect to each other, therefore allowing the cell number to be unambiguously defined by the signal timing. The delays are measured regularly during data taking and a hit resolution of about 800 μm is achieved. A logical OR of all wires in the plane is read-out by a 1 ns TDC. Such a precise measurement is useful for cross-calibration of 10 ns TDCs, and supersedes low-resolution measurements in the case of a single track.

All cathode strips have individual analog read-out channels, with the charge digitized by dual-range flash ADCs. Clusters with two and more neighbouring strips having signals above the threshold are used for subsequent analysis. The resulting effective hit efficiency for the strip read-out is (80 ± 2)%. The induced charge distribution is virtually independent of the cluster width, with 95% of the charge contained in three central strips. Therefore, the cluster center-of-gravity is calculated using only the maximum-charge strip and its two neighbouring strips. The relatively high noise rate, due to the absence of front-end preamplifiers, limits the hit resolution to 2.4 mm (rms) per plane for the streamer chambers strip read-out. However, this is sufficient to provide a constraint for right–left ambiguity in the streamer tube drift-distance measurement, as well as a measurement in the case of wire read-out inefficiencies or failures.

Streamer chambers are also used in the other parts of the experiment for tracking purposes. There are 4 planes in front of the veto scintillators, 6 planes called the "Tracker Streamer Tubes" (TST) (only 4 planes in the 1994 run), between the trigger H-hodoscopes (see Section 9) and the calorimeter, and 22 planes interleaved between the calorimeter planes. Originally, all these planes had only a digital read-out. In 1995 the TST planes were upgraded by adding a drift-time read-out with 1 ns TDCs. In August 1996 the TST planes were replaced by the honeycomb trackers described in Section 14.1.

The methods of track finding and track fitting for the muon spectrometer are described in Ref. [25].

8.4. Scintillators

The scintillators embedded in the magnets are mainly used for triggering and to detect possible energy leakage from the calorimeter, for special types of events. In addition, a measurement of the momentum of muons which range out inside the spectrometer (< 5 GeV/c at the entrance to the spectrometer) is performed using the sampling of the iron by the scintillator planes.

Each scintillator layer in a magnet consists of 24 strips of 15 cm width, each consisting of two independent halves separated by a mirror. Five consecutive layers have the same (horizontal or vertical) strip orientation and form a read-out plane. Every five consecutive half-strips in the beam direction form "half-counters" viewed by a single PM [22]. Thus, each magnetic module has four read-out planes, two with vertical and two with horizontal "counters". The light attenuation in scintillators, aged after 15 years since the magnets were built, is fairly strong (the yield varies by factor $\sim$ 5 over 180 cm long central half-counters).

After summing the signals from opposite half-counters, 90% of the sum signals is fed into ADCs and 10% is used for triggering. The original CDHS trigger electronics has been upgraded to provide a wider set of primary trigger signals, which are used in the central trigger decision logic (Section 9) as well as in stand-alone subsystem triggers. The efficiencies of the trigger signals are close to 100%.

The first two spectrometer modules serve as a hadronic shower tail catcher for the calorimeter.

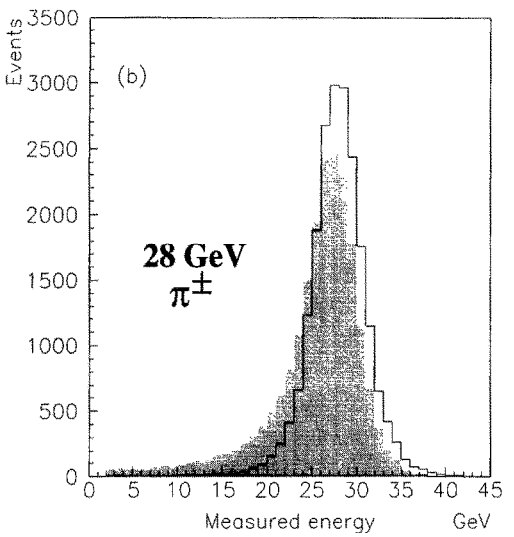

Fig. 23. Reconstructed energy distributions for 28 GeV test beam pions. Shaded histogram: the calorimeter measurement alone (25.5 GeV (mean) ± 5.3 GeV (rms)), solid line: the sum of the calorimeter and the muon spectrometer measurements (27.9 GeV (mean) ± 3.2 GeV (rms)).

For events having a longitudinal shower leakage, the total shower energy is reconstructed by adding up the calorimeter and muon spectrometer measurements, properly intercalibrated. The spectrometer energy resolution for shower tails above 1 GeV is $(110–150\%)/\sqrt{E(\mathrm{GeV})}$ (Section 12.3). Fig. 23 illustrates the effect of the shower leakage correction for the case of a significant leakage, typical of "calorimeter" triggers (Section 9). For "main" neutrino triggers, with the leakage not exceeding 2% of the shower energy, the correction is not applied.

9. The trigger system

The principal task of the trigger system is to select neutrino interactions in the emulsion target region. The other important task is the sequencing of data taking with the time structure of the neutrino beam. The main difficulties arise from the need to form a "strobe" with no incoming charged particle and from the limit of 2 events per neutrino spill imposed by the CCD optoelectronic read-out. The calorimeter and muon spectrometer also act as a neutrino target in which more than one hundred events per neutrino spill originate. Only about five of these are selected per spill.

The scintillator trigger-hodoscopes E, T, H, V and A, shown in Fig. 24, are used to select neutrino interactions in the target and to reject background from cosmic rays, beam muons and neutrino interactions outside the target. A neutrino trigger in the target region (the "main" trigger) is defined by a hit coincidence in E, T and H consistent with a particle trajectory with $\tan\theta < 0.25$ w.r.t. the neutrino beam axis.

A veto is formed by any combination of a counter hit in the veto hodoscopes (V and A) and a hit in T, with precise timing to avoid vetoes due to backscattering, as depicted in Fig. 25. The T and V scintillator strips are coupled on both sides to a photomultiplier. Photomultiplier signals are discriminated by a CAMAC constant fraction discriminator with 200 ps "time walk". A position independent signal is then provided by a CAMAC mean timer, allowing a maximum relative delay between the first and second discriminator pulse of 50 ns and a timing resolution of 200 ps. The veto timing resolution thus achieved is 2 ns at FWHM.

The veto inefficiency at the level of 10^{-3} is essential to reject beam-related incoming muons. The muon flux incident on the detector during the neutrino beam operation is measured to be $N_\mu \approx 18/\mathrm{m}^2$ per 10^{13} protons on target.

The measured rate of neutrino interactions is 0.5 events per 10^{13} protons on the SPS target corresponding to an effective neutrino target mass of 1600 kg. The fraction of those events originating in the emulsion target is 50%. (In 1994, when the E-hodoscope plane was not yet installed, the triggerable mass was 2000 kg, out of which 40% of the interactions originated from the emulsion target.) The cosmic background is very small, about one $T \times H \times \bar{V}$ coincidence per 100 ms. Owing to the high redundancy of the trigger system and to the simplicity of requirements, a trigger efficiency of 99% (>90%) was measured for ν_μ charged (neutral) current events passing the off-line selection criteria.

Table 2 summarizes the trigger hodoscope characteristics. The E hodoscope system is made of two staggered planes of seven 20 cm wide scintillators oriented vertically. As shown in Fig. 3, it is located 20 cm downstream of the emulsion target between target tracker modules 6 and 7. Being mounted as

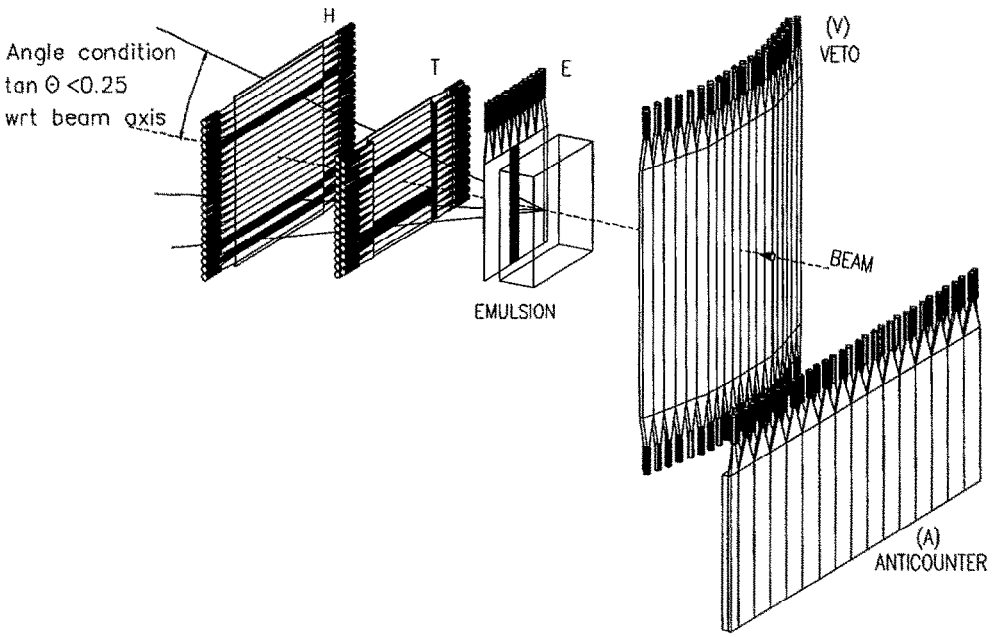

Fig. 24. Schematic layout of the trigger hodoscopes.

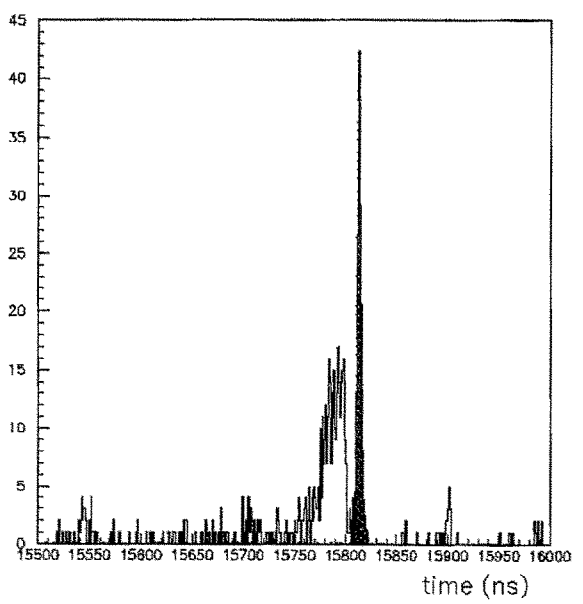

Fig. 25. The measured time correlation between hits in the trigger plane T and in the veto plane V. The shaded peak is due to tracks in the beam direction, while the other events are from back-scattered tracks which can be separated.

close as possible to the exit of the emulsion target, it rejects neutrino interactions occurring in the iron support structure of the target region and in the image intensifier chains used to read-out the fiber trackers. The T system is made of two staggered planes of 15 scintillator strips of 10 cm width and 160 cm length, oriented horizontally. It is located after the last target tracker module. The thickness of the E and T hodoscope modules (1 cm) minimizes the loss of tracking precision due to multiple scattering. The trigger plane H, positioned in front of the calorimeter, consists of two staggered planes of 20 strips of 10 cm width and 200 cm length, oriented horizontally.

The veto system V is installed 2 m upstream of the target region and consists of two staggered planes of twenty 20 cm wide scintillators oriented vertically. It covers an area of 3.2×4 m^2, large enough to screen beam related muons and to suppress triggers produced by incoming muons. An additional anticounter A hodoscope made of 2 planes of 16 scintillators 20 cm wide vetoes events due to interactions in the concrete floor, reducing the total trigger rate by 13%. It is positioned below the V plane and behind a 10 cm

Table 2
Characteristics of trigger hodoscopes

	E	T	H	V	A
No. strips/plane	7	15	20	20	16
Strip width (cm)	20	10	10	20	20
Strip length (cm)	148	160	200	320	200
Area covered (cm^2)	150 × 148	160 × 160	200 × 200	400 × 320	200 × 320

iron wall which absorbs soft backscattered particles from the emulsion target.

In addition to the main triggers, several other triggers were implemented, such as an alignment trigger, a quasi-elastic neutrino event trigger in the calorimeter allowing the measurement of the neutrino energy spectrum, and a dimuon trigger for charm physics studies of events produced in the calorimeter or in the spectrometer. A total of 16 different trigger types can be handled. Calorimeter and spectrometer triggers do not require the read-out of the optoelectronics subsystem.

The trigger decision is made in four steps. The first one is provided by a so-called strobe signal. In the case of a neutrino interaction in the emulsion target, the main strobe is formed by a simple coincidence of T and H scintillator planes with a rate of about 40 strobes per 10^{13} protons on target. The strobe logic for the other triggers is a simple coincidence from the calorimeter and the spectrometer, which is mixed with the main strobe. Their rate is about 300 strobes per 10^{13} protons on target.

The strobe signal provides the timing signal to start the pretrigger, which makes a fast decision by checking a minimum set of conditions. For example, the main physics trigger requires a coincidence of the strobe and neutrino physics gate and no activity in the veto planes.

In the next step the main trigger decision is initiated. A complex chain of VME-Programmable Logic Units with high speed look-up memories (12 ns) processes the decision input signals. The strobe latches the input data and generates the corresponding output pattern within 20 ns. Low level patterns are determined based on detector signals which allows counting number of planes, checking vetoes, applying fiducial volumes. The trigger condition for the T and H scintillator planes is performed by a custom designed dual width VME-Hodoscope Logic Unit. This unit accepts 30 T inputs and 40 H inputs, applies a logic matrix operation on the input patterns and generates an output signal if the particle trajectory is consistent with $\tan\theta < 0.25$ with respect to the neutrino beam.

The final trigger pattern combinations are then calculated and sent to a VME-Logic Matrix Unit. Coupled with the other pre-defined parameters like the scale-down factors, this information is translated into a 16-bit trigger pattern. Each bit corresponds to a different read-out pattern, allowing for a different set of subdetectors to be read out for different triggers. The total decision time is about 100 ns.

Some triggers have to be validated by a specific enable signal to generate the corresponding readout signal and thus can be downscaled. The frequency of the enable signal defines the downscaling factor desired and the validation is made by the coincidence of trigger bit and enable signal at the input of the Logic Matrix Unit (LMU).

In the 14.4 s cycle of the SPS accelerator there are two 6 ms neutrino spills, separated by 2.7 s, as depicted in Fig. 4. The data taking modes of the detector are synchronized to the accelerator cycle with the help of a hardware interrupt handler and timing signals from the accelerator. In the long interburst period, control is given to the subdetectors which can take calibration events, each using a simple local trigger. When a timing signal from the accelerator arrives, an interrupt is generated and control is given to the trigger system. During the neutrino spill, the trigger processor detects hardware triggers by polling the inputs of the interrupt handler. The essential trigger conditions are read from the LMU and stored. If necessary, new trigger conditions can be set in the LMU within 15 μs. This allows to control the event limit of different subdetectors in order to respect buffer sizes and to control the busy status of the CCDs. The software can perform this task within the conversion time of the digitization and therefore this operation does not contribute to the overall deadtime. At the end of the spill, the steering

software sends a list of event descriptors to the event builder, which can then organize the read-out of all subdetectors.

The deadtime of the experiment is of about 10% in a typical neutrino spill of 6 ms width and 10^{13} protons on target. The main sources are the CCD conversion and read-out time (6%, of which 3% is due to the maximum limit of two events) and the ADC/TDC conversion time of about 20 μs for an average rate of 5 events/spill (3%). The activity in the veto counters and the total strobe rate account for the remaining 1%. The information used for the deadtime calculation, weighed with the neutrino spill structure, is stored in specially designed VME Buffered Scalers with 2 k event deep memory. The beam muon rate as measured inside the shielding, which is proportional to the neutrino flux, is counted in time slices of 100 μs. It provides information on the neutrino spill time structure and the time dependence of the deadtime. The individual sources of deadtime per trigger are also measured with the help of a VME Buffered Pattern Unit with 4 k event deep memory. The input pattern, containing signals relevant for deadtime calculations, is latched by pulses generated by muons in the neutrino beam.

During the 15 μs gate time of the MCPs, a second neutrino interaction may occur with a probability of the order of 10^{-3}. This event is not triggered because the previous one is still being processed, but it causes an overlay of pictures/tracks in the CCD image active area. To account for these cases, the time of each hit in the trigger scintillator counters is stored (for each event) in TDCs with multihit capabilities (16 hits/channel) and 64 μs full dynamic range. In addition, the hit pattern in all the trigger scintillator planes is recorded in VME Buffered Pattern Unit for every strobe, formed by a simple coincidence of T and H scintillator planes. The correlation between the time of each hit and the hit pattern in the trigger planes therefore helps in identifying the occurrence of a double event and to flag particle trajectories.

10. Data acquisition and on-line facilities

The CHORUS data acquisition (DAQ) [26] is constructed as much as possible on machines running a standard UNIX operating system. For the low-level "real-time" parts, however, an operating system is needed that can guarantee sufficiently short interrupt response times. At the time when the DAQ system was designed, the OS-9[22] real-time kernel was the most viable system with that property, so this system was chosen to read-out the CHORUS VME modules.

The essence of the DAQ hardware is formed by a tree of VME CPUs, interconnected via the VME Inter Crate (VIC) bus,[23] as well as the Ethernet, as shown schematically in Fig. 26. The branches of the tree are formed by the four detector subsystems: optoelectronics (OPTO), trigger (TRIG), calorimeter (CALO), and spectrometer (SPEC). Data are collected at the root of the tree by the event builder (EVB).

Each subsystem runs a local DAQ on its main crate controller.[24] The local DAQ is equipped with a local trigger system, such that the subsystem can be operated in stand-alone mode. In that case its global VIC bus connection is switched off-line. Besides VME, the local DAQ may use VSB and CAMAC systems. The OPTO subsystem contains 29 SL30 image processors that read and compress the data from the CCD cameras and send the result to the OPTO main crate controller through a local VIC bus. The compression factor achieved is about 100.

Each main crate controller runs the OS-9 real-time kernel, together with a set of server processes for the communication over the VIC bus. These processes implement REMOS (REMote Operating System[25]), which manages remote shared memory. Besides the global REMOS, the OPTO and SPEC subsystems each have a private instance of REMOS, used by the various processors within the subsystem, as shown in Fig. 27. REMOS and the DAQ programs have essentially been implemented in the object oriented C++ language. The DAQ programs are structured as Finite State Machines, for which a general purpose language on top of C++ was designed and implemented. The resulting software has proven to be versatile and scalable.

In global mode, the data from the subsystems are assembled into complete global events on the EVB. In

[22] OS-9 System, Microware Systems Corporation, USA.

[23] VIC-8251, CES, Switzerland.

[24] FIC-8234, CES, Switzerland.

[25] REMOS – G. Carnevale et al., in "Procs. of CHEP'94 Conf.", 311, San Francisco.

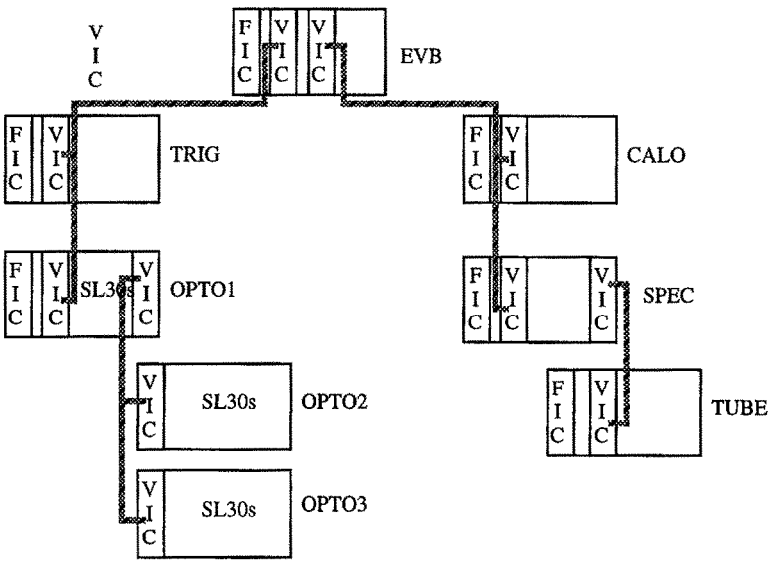

Fig. 26. The schematics of the VME hardware tree of the CHORUS data acquisition system.

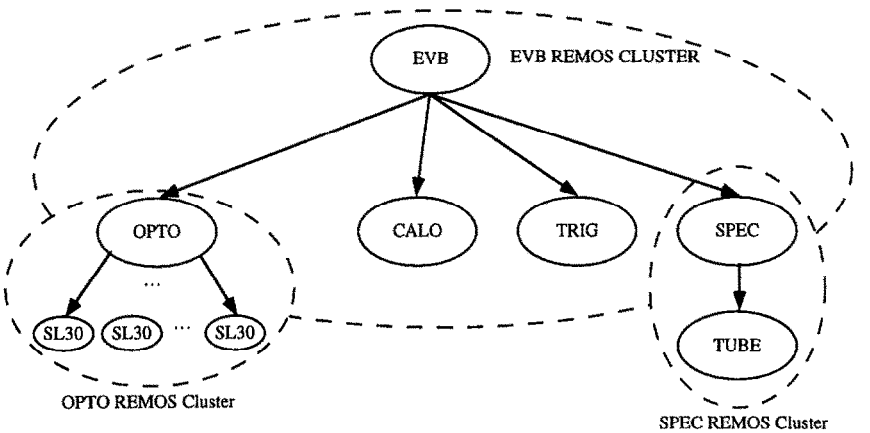

Fig. 27. The connection between global and local remote operating systems in the CHORUS data acquisition system.

this case the TRIG subsystem has recorded event-by-event which subsystems participated in the read-out, and only those subsystems are contacted by the EVB to deliver their data. In stand-alone mode, each subsystem is independent. In either case the full events are sent as messages via VSB or Ethernet to a dispatcher process on a UNIX (AIX) machine, that makes the data available to client programs, via shared memory or Ethernet.

The dispatcher[26] is a general-purpose message-based data distribution program. When a client opens a connection to a dispatcher, it subscribes itself to a list of message tags. A tag indicates the type of the data contained in a particular message. Whenever a message is sent to the dispatcher, a copy is made

[26] Dispatcher – R. Gurin and A. Maslennikov, CHORUS Internal notes, 1995.

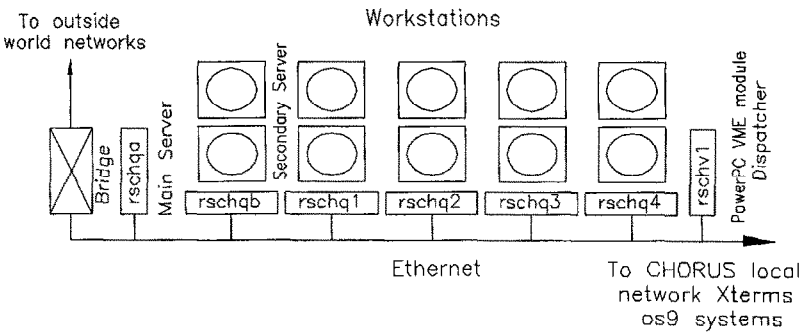

Fig. 28. Overview of the UNIX workstations in the CHORUS data acquisition system.

available to those clients that are subscribed to the corresponding tag. Messages are also used to send commands to DAQ programs. For example, status inquiry commands are used by a supervisor program to monitor vital components of the DAQ system. The supervisor has been implemented in the "expect"[27] interpreter.

The experiment is controlled from five IBM RS-6000 PowerPC workstations (see Fig. 28), typically by means of a graphical panel. This panel has been implemented in the Tcl/Tk[28] interpreter. When a subsystem is being run in stand-alone mode, it can be controlled by the very same panel software, now configured for the stand-alone mode requested. In that case the remaining subsystems still can run a global DAQ from the global panel, but without the subsystem in question.

Each workstation is equipped with two large graphical screens, displaying windows containing histograms and other results from data monitoring programs. All these programs are in general clients of a dispatcher. A "logger" displays the messages that are being sent by DAQ programs. Various automatic histograms continuously show the activity in the subsystems during data taking. From these histograms malfunctioning channels (inactive or noisy) can be identified. The complete history of such histograms is accessible through the on-line monitoring archive. Another important client is the on-line display of reconstructed events. This program displays hits and reconstructed tracks in a model picture of the CHORUS detector. There are also windows which display the event rates for triggers of various types, the associated deadtime percentages, as well as the structure and timing of each neutrino spill.

Closely related to the DAQ is the "slow control" system [27], which monitors hardware parameters that may change during data taking. These parameters include the low and high voltages of the detectors and their read-out hardware, temperatures, gas flows, etc. The OS-9 system is again used for the low-level DAQ. The main crate controller is used to read-out VME-based monitoring modules, like CAENET[29] high voltage controllers. Furthermore there is an interface to a G-64[30] crate housing a CERN-built monitoring system used previously in the CHARM II experiment [23]. This system is based on voltage-to-frequency converters and pulse counters. In either case the measured values are sent via the Ethernet to a dispatcher. A client program written in Tcl/Tk then displays the status of all the 4589 monitored channels, and saves their history on disk. Each channel is checked every 2 min. An alarm is generated for any channel whose value lies outside its allowed range.

For precise monitoring of the neutrino beam, data are collected from detectors operated by the SPS West Area Neutrino Facility group, who use a DAQ system controlled by the commercial product FactoryLink [8]. A workstation running a graphical interface to FactoryLink displays various histograms

[27] Expect – "Exploring Expect", D. Libes, O'Reilly & Associates, 1995.

[28] Tcl/Tk – "Tcl and the Tk Toolkit", J.K. Ousterhout, Addison-Wesley, 1994.

[29] CAENET – CAEN, Italy.

[30] G-64 – PEP Modular Computers, Switzerland.

and profiles, providing monitoring facilities for the neutrino beam performance. It also allows limited control of the beam line, such as resetting a tripped magnet. The recorded beam data are made available via the Ethernet to the CHORUS beam histogram task.

In the 1994–1995 data taking, global events were written on 200 Mbyte IBM 3480 tapes, operated by a drive directly connected to the EVB. Stand-alone events were written to a local Exabyte drive, or to an NFS-mounted disk. Starting from the 1996 data taking, the events are saved first on disk by one of the dispatcher clients. As soon as a run has finished (typical duration 90 min), the resulting file is sent over the network to the off-line computers. Also it is backed-up immediately on a local 10 Gbyte DLT drive.

During each of the two neutrino spills per SPS cycle, typically 5 global events are recorded in 6 ms and have to be processed in about 1 s. The corresponding amount of data is less than 250 kbytes on average, but it can be as large as 2 Mbytes when the OPTO subsystem is involved. In the 12 s interburst period, each subsystem can take local events. The combined local data rate is less than 50 kbytes/s on average.

11. Emulsion handling and scanning

Nuclear emulsion is a continuously sensitive medium, and therefore records all charged particle tracks due to cosmic rays and ambient radioactivity that have crossed the detector between pouring and processing. Background piles-up and makes the scanning inefficient beyond a certain space track density. Therefore, pouring of gel and processing of exposed emulsion takes place at CERN to minimize unnecessary background accumulation. The total time interval the emulsions are active is about 1.5 yr, during which there are two times six months of exposure in the neutrino beam. Great care has been taken throughout the emulsion handling procedures to minimize local stress in the emulsion plates, which may cause distortion undesirable to the subsequent scanning analysis.

The pouring facility at CERN was built for the experiment WA75 [28] and has been then upgraded for the exceptional requirements of the CHORUS experiment. Under standard conditions, a pouring rate of 26 l of emulsion per week has been achieved. The production of the 770 kg (206 l) of the emulsion target and of the other associated interface emulsion sheets requires 3 tons of nuclear emulsion gel and takes 3 months to complete.

After the exposure of the emulsion stacks in the neutrino beam, a precise map of fiducial marks is printed on all the emulsion plates, to be used as an internal reference. The processing is done at CERN in the existing facility, upgraded for CHORUS in order to handle large-size double-coated plates. A processing rate of 17 l per week is achieved, with a "hot" (24°C) wet stage and by using amidol as developer. Four months are needed to treat all the emulsion.

Scanning of the emulsion plates is peformed by both "semi-automatic" and "automatic" systems. The semi-automatic scanning procedure, employing the so called "mini-plate" method, is a conventional technique already used in previous experiments [12]. The automatic scanning system [13] is a new technology developed during the course of the experiment. The schematic diagram of the first operational version is depicted in Fig. 29. The entire emulsion plate ($36 \times 71\ \mathrm{cm}^2$ for the interface sheets, and $36 \times 35.5\ \mathrm{cm}^2$ for the target sheets) is placed on the microscope stage and kept flat by vacuum. Immersion oil is put on the surface of the emulsion plate to optimize the light illumination of the microscope objective lenses. Intercalibration between the microscope and the emulsion plate coordinates is achieved by means of fiducial marks. The microscope image is read-out by a CCD camera.

The emulsion provides three-dimensional images of the trajectories with a grain ("hit") size of 1 μm and an average density of 300–400 hits per millimeter for minimum ionizing particles. A video image of a typical neutrino vertex is shown in Fig. 30. The dimension of the view is about $120 \times 100\ \mu\mathrm{m}^2$, while the focal depth is only a few microns. The thick tracks correspond to large-angle low-energy hadrons or nuclear fragments, emitted almost perpendicularly to the beam axis. High energy particles which traverse the plate in the forward direction are not clearly viewed in one focal plane, and manifest themselves only as the shadowy tracks from the vertex. The scanning system drives the microscope stage to the predicted position and detects the surface of the emulsion plate automatically (autofocus). After this, the image data taking with synchronized depth driving starts.

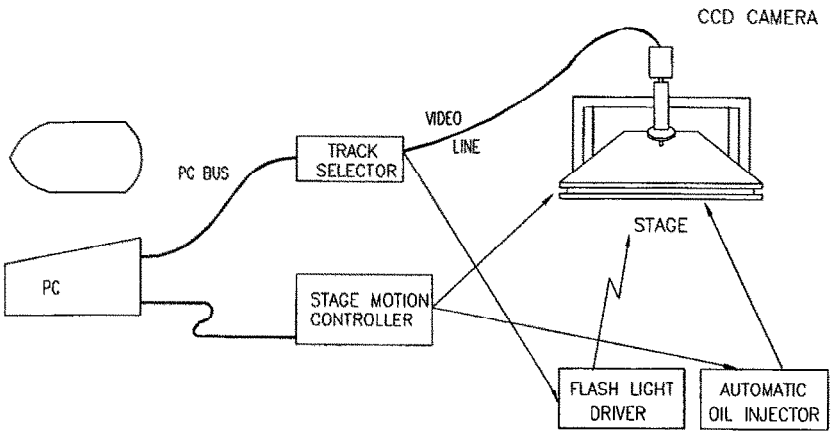

Fig. 29. Schematics of an automatic emulsion scanning system.

Fig. 30. The video image of a typical neutrino vertex. The dimension of the view is $120 \times 100\,\mu m^2$, while the focal depth is a few micron.

The basic idea of the automatic scanning system shown in Fig. 30 is described schematically in Fig. 31. The three-dimensional information of the emulsion is converted into many layers of a tomographical image by the synchronized interplay between the microscope and the CCD camera. Each tomographical image is focused on some depth and covers an area of $150 \times 120\,\mu m^2$. The "Track Selector" is a real-time processor which digitizes the CCD video signals and sends the 512×480 pixels of data (each having 4 bits) into a dynamic frame memory. Sixteen layers of digitized images are stored, and the predicted tracks are located by superimposing the data with different shifts between layers. A track is identified by having an enhancement in the superimposed signals when the shifts match the angle of the track. Found tracks are then followed to the next emulsion plate, until the neutrino interaction vertices are located.

Fig. 32 displays the "plate-to-plate" following efficiency among the target emulsion plates (350 μm thick on both sides of a backing plate). The inefficiencies are mainly due to the stains and fiducial marks on the surface of the sheets. The angular resolution of the Track Selector depends on the thickness of the emulsion plates. In particular, for a 100 μm thick plate (CS or SS) the angular resolution is measured to be about 4 mrad. By combining the track position in the front and back surfaces of the backing plate, an angular resolution of 1 mrad can be achieved for the changeable and special sheets, which have 800 μm backing plates. The typical time required to process one microscope view (corresponding to an area of $150 \times 120\,\mu m^2$) is about 4 s. This includes the digitization of each track, the movement of the stage and the detection of the emulsion surface. R&D efforts are being pursued in the Collaboration [29] and improvements in the scanning speed are expected for the near future.

12. Detector calibration procedure

Cosmic-ray events are taken, during the 12 s SPS-interburst interval, to calibrate different elements of the detectors and to monitor time variations of the

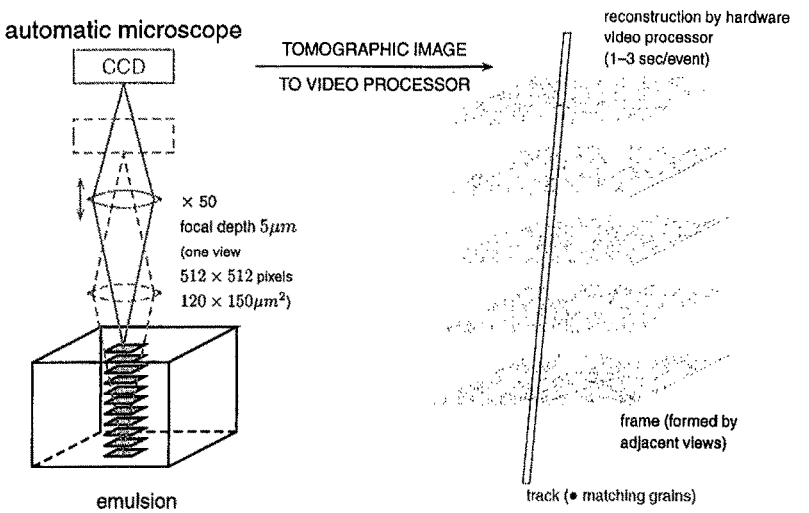

Fig. 31. Schematic description of the track reconstruction procedure in the automatic scanning system of Fig. 29

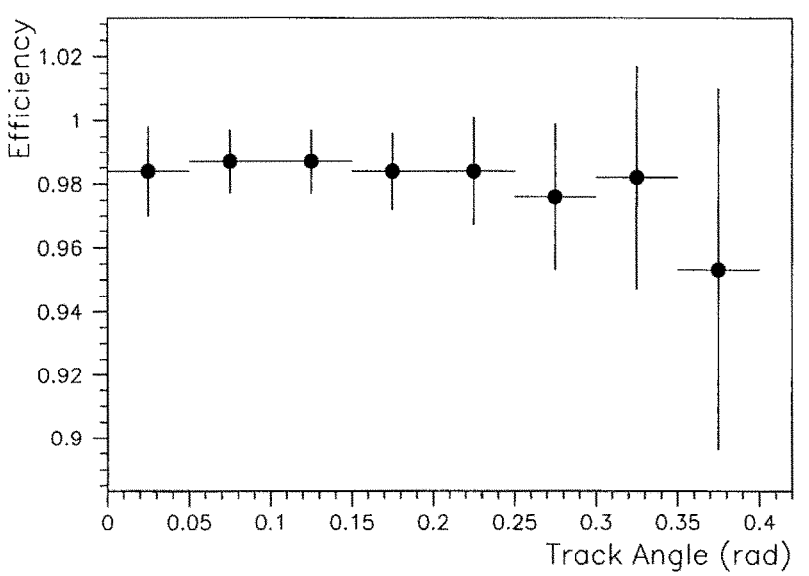

Fig. 32. The measured "plate-to-plate" following efficiency among the target emulsion plates.

response. In addition, the calorimeter and the spectrometer need an "absolute" calibration in energy or momentum. Therefore, test beams of electrons, muons and pions have been used to determine their absolute energy/momentum scale. Data from the penetrating high-momentum muons associated with the neutrino beam are also taken without the air-core magnet pulsing, typically once per month, to monitor the relative alignment of the various detectors.

12.1. Calibration of the fiber tracker system

The high-momentum muons associated with the neutrino beam are used for monitoring the response of the fiber tracker system, namely the light yield, the attenuation length, the spatial resolution and ageing effects, as well as to perform precise transverse alignment between the different tracker planes. Longitudinal alignment of the tracker planes is based on cosmic-ray tracks taken during the interburst intervals.

The response of the optoelectronic read-out devices is monitored independently of the scintillating fibers by the "fiducials" calibration system as described in Section 5.2. Data from LED flashes in the fiducial fibers are taken during the interburst intervals, and are used to correct the image distortion as well as to monitor the efficiencies and the spatial resolution of the read-out chains.

12.2. Calibration of the calorimeter

Three steps are needed for the determination of the calorimeter response:

- Equalization of the signals from each individual photomultiplier (PM) within each sector (EM, HAD1 and HAD2), performed by measurements with penetrating cosmic rays. An equalization constant is computed for each PM by selecting cosmic muons crossing the central region of the modules (± 10 cm), and correcting for the effective track length. The statistical error for this procedure is at a $\pm 5\%$ level, while the systematic effects due to the time dependence of the PM gain and to the position dependence of the energy response are less than 3%. Cosmic-ray events are also used to create a data base of the malfunctioning PMs (inactive or noisy) during the running periods, and for the on-line monitoring of the calorimeter.
- Intercalibration among different sectors. To combine the signals of the three different sectors, two intercalibration constants are needed, namely those of HAD1 and HAD2 relative to EM. These constants are determined experimentally using pions of known momentum interacting at different calorimeter depths, and studying the sharing of the shower energy between different sectors [21].
- Overall energy calibration. The calorimeter response to the incoming particles is determined by adding-up the energy deposited in all the modules, once the equalization and intercalibration procedures previously described have been performed. Each module is equipped with PMs on either side. Therefore, there are different possible definitions of the energy deposition, according to the ways the two PM signals (L and R) are combined. The geometric mean $S_g = \sqrt{S_L \times S_R}$ is chosen since its response (hence the energy derived) is independent of the hit position along the length of the module. For the channels which are noisy or inactive during the data taking, the signal from the other PM on the same module is used, after correcting for the light attenuation based on the hit position.

The measured shape signal-distribution of the calorimeter as obtained with pions is well fitted to a Gaussian. Therefore, the calibration and intercalibration procedure do not introduce any appreciable bias in the determination of the overall calorimeter response.

The results on the energy calibration of the calorimeter have already been presented in Section 7. In addition, a "direct" pion beam (X7) is also exploited for calibration purposes. These pions, which are parallel to the neutrino beam axis and hit the target region, can interact and start showering in the emulsion stacks or in the downstream calorimeter. From the study of those events sharing the shower energy between the two detectors one can "cross-calibrate" the lead calorimeter and the target region. Using the energy depositions sampled by the fiber tracker modules, it is then possible to partially

recover the energy loss upstream of the lead calorimeter [30].

12.3. Calibration of the spectrometer

Negative muons of 75 GeV/c momentum from the SPS West Area are used to calibrate the momentum measurement of the muon spectrometer. Due to ionization losses in the upstream detectors and beam elements, the beam momentum is about 71 GeV/c at the entrance of the spectrometer. Monte Carlo simulated muons are used at other momenta to obtain the momentum dependence of the muon momentum resolution (Fig. 22). The latter is determined by a Gaussian fit to a reconstructed (1/p)-distribution for a given incoming muon momentum. The measured resolution at 71 GeV/c is by 2% worse than the one predicted by the Monte Carlo simulation, which can be attributed to a small residual drift chamber misalignment. At very low momenta (1–5 GeV/c) the momentum scale is confirmed using the range of stopping muons. The resolution for stopping muons (6% on average) was estimated by comparing the nominal momentum of simulated muons with the value determined by their range.

Cosmic muons recorded in the interburst are used for the scintillation counter equalization and for the determination of the light attenuation curves. The correction for the light attenuation is needed because, unlike in the calorimeter, the counters are equipped with a PM on one end only, and with a mirror installed on the other end. Cosmic rays are also used for the on-line monitoring of the efficiencies of all the spectrometer elements.

To measure the shower energy leaking from the calorimeter, the first two spectrometer modules are calibrated relative to the calorimeter. The method is similar to the intercalibration of different calorimeter sectors. It is based on studying the sharing of the deposited shower energy between the entire calorimeter and the spectrometer, for test beam pions of known energies interacting at different calorimeter depths. The resulting energy calibration of the spectrometer response, obtained with 7–28 GeV test beam pions, is shown in Fig. 33(a). The spectrometer energy resolution for hadronic shower tails is estimated by a deconvolution of the combined energy resolution, using the known hadronic energy resolution of the calorimeter (Section 7.2). To obtain the energy dependence of the resolution, this analysis is done for narrow intervals in E_S, the energy measured in the spectrometer. The result is presented in Fig. 33(b), where each dot corresponds to the average resolution obtained for shower tails from 15, 20 and 28 GeV test beam pions.

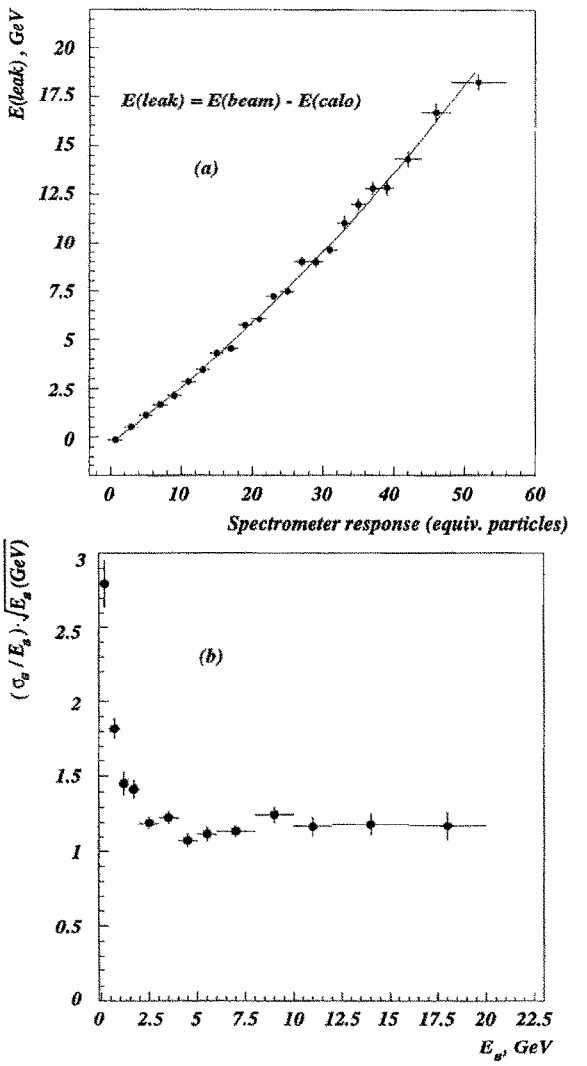

Fig. 33. (a) Spectrometer scintillator calibration. E (leak), the difference between the nominal beam energy and the energy measured in the calorimeter, as a function of the measured spectrometer response (in equivalent particles). (b) Spectrometer scintillator energy resolution for hadronic shower tails, expressed as $(\sigma_S/E_S)\sqrt{E_S}$, against the energy measured in the spectrometer, E_S.

The mutual alignment of the spectrometer components (drift chamber planes, streamer tubes, cathode strips and the scintillators) is done with 100 GeV/c test beam muons recorded with the magnetic field turned off. The global alignment relative to the rest of the CHORUS detector is done by reconstructing high-momentum neutrino beam-related muons traversing the entire detector. These "alignment" events are also used for precise "time-zero" calibrations needed for drift-time measurements.

13. Data handling and analysis

The raw data of a typical running year amount to about 400 Gbytes, including both physics triggers (with or without signals from the scintillating fiber trackers), and local calibration events. The latter are split-off and written to separate data streams on high-capacity tapes (IBM 3590), where they are made available for calibration of the different detectors.

An analysis program package called CHORAL has been developed for the event reconstruction from the the raw data. Event visualization is performed by an interactive version of this program, providing facilities for the step-by-step processing of each event.

The pattern recognition of the event topology starts independently in the fiber tracker area and in the region of the muon spectrometer. An unbiased search of three-dimensional straight tracks is made in the target trackers in the gaps between emulsion stacks 2 and 3 and downstream of stack 4, where 12 fiber planes are located in each case. These track segments are extrapolated to the vertex in the upstream direction, and into the region around the hexagonal magnet in the downstream direction. The vertex is defined by a three-dimensional matching condition for the tracks. A momentum fit is performed for tracks from the vertex which can be followed to the magnet tracker modules downstream of the air-core magnet.

In the muon spectrometer, the tracking and the measurements of the momentum and charge of the muon candidate is performed by combining track segments in the different tracking gaps. The tracks are followed upstream through the calorimeter. At the entrance face of the calorimeter, both track types are compared and matched. This allows for an efficient flagging of muons at the vertex. Calorimetric information is supplied by measuring the total shower energy and direction in the calorimeter. A correction can be applied for the energy lost in the emulsion region, and for the (minor) shower leakage into the muon spectrometer. For isolated tracks, the energy profile in the calorimeter is deduced independently, allowing for particle identification.

Entry points and directions at the interface emulsion sheets for all reconstructed tracks associated to the vertex are calculated. Emulsion scanning is performed based on these predictions. The found tracks are then extrapolated and searched for in the special sheets. The track is followed into the target emulsion until the plate where the interaction vertex takes place. All tracks emerging from the vertex are then measured, and the possible decay topologies (kinks and stars) are subsequently identified.

The results of the topological event reconstruction are stored on high-capacity tapes in a compact Data Summary Tape (DST) format which allows for systematic inclusion of the scanning results at a later point in time, and for a limited number of reconstruction algorithms to be re-applied, if necessary. Track predictions for emulsion scanning are written to a far smaller data set, which can be transferred over wide area networks between CERN and the scanning laboratories of the Collaboration.

Event reconstruction is performed on UNIX machines in the CERN computer center, running the IBM AIX operating system. For event simulation, Unix machines both at CERN and in other collaboratins institutes are exploited, running IBM AIX, HP-UX and Digital Unix. All programs have been made to work under Digital's VMS and IBM's VM-CMS operating systems as well. The vast majority of the programs is written in Fortran77, making use of standard facilities of the CERN program library.

14. Detector upgrade for the 1996–1997 run

14.1. The honeycomb tracker

Three "honeycomb" [31] tracker chambers have been built and installed in the CHORUS apparatus for the 1996–1997 data taking. Their main task is to

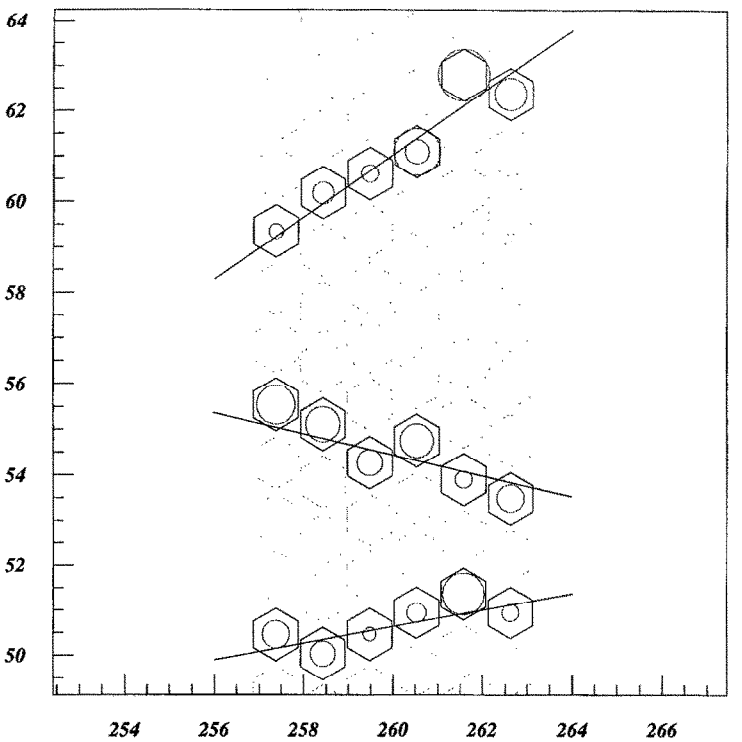

Fig. 34. Display of the hit pattern of tracks in one honeycomb chamber. The $x(y)$-axis corresponds to the beam (vertical) direction; the units are in cm. The hits are represented as circles around the central wire position.

complement the existing magnet trackers by providing a module with independent tracking capabilities at a similar spatial resolution. The streamer-tube trackers (TST) located between the trigger H-hodoscope planes and the calorimeter have been replaced by the new honeycomb trackers in August 1996. The honeycomb chambers consist of hexagonal cells, each cell acting as a single-wire drift chamber with a measured relation between space and drift time.

The chambers are mounted at 60°, 0° and 120°, respectively. Each chamber consists of six planes, and each plane contains three identical 1 m wide modules with the drift cells coupled longitudinally, so forming 216 drift cells with a wire spacing of 11 mm. The total area is $3 \times 2.75\,m^2$, matching the aperture of the hexagonal magnet. The planes are staggered such that the inefficiency due to the dead area between chamber cells is minimized. The gas is a 1 : 1 mixture of Ar and CO_2. Relative alignment between the honeycomb tracker and the magnet tracker is achieved by a RASNIK device [32].

On each chamber, the analog signals are amplified and digitized by a time-over-threshold discriminator in 18 front-end electronic cards every 5 ns, and the output is stored in a single page of a memory. A central trigger increments the page counter of the memory. At the same time, the last memory address is stored in a FIFO. After each neutrino spill, each occupied memory page is read-out circularly starting after the location pointed to by the corresponding data in the FIFO. An event with tracks in one of the honeycomb detector planes is shown in Fig. 34.

14.2. The emulsion trackers

In addition to the magnet trackers, the air-core hexagonal magnet region has been equipped with

emulsion trackers for the 1996 and 1997 runs. The aim is to improve the momentum accuracy and to extend the range of measurement from 10 to 30 GeV/c, a kinematical domain which includes an additional 26% of the $\tau^- \rightarrow h^- X$ events.

Three such trackers, labelled ET0, ET1 and ET2 in Fig. 9, have been installed. The first is placed immediately downstream of the target tracking region, while the others are in the space between the magnet and the neighbouring magnet trackers.

ET0 is composed of 8 juxtaposed emulsion sheets, while both ET1 and ET2 have 18 sheets. Each sheet has an emulsion layer of 70 μm on both sides of a 800 μm thick $74 \times 37\,cm^2$ Lucite support. Sheets are attached by vacuum to a 20 mm thick honeycomb panel. The position of each sheet relative to the honeycomb board is known with an accuracy of 30 μm by using 18 ^{55}Fe X-ray guns embedded in the honeycomb board. The sheets are replaced twice a year to limit the background due to passing through tracks.

Only secondary tracks from τ^- decay candidate events are searched for in the emulsion sheets, in a scanning area of $2 \times 2\,mm^2$ around the position predicted by the scintillating fiber trackers. This area is inferred from a test run performed in 1994, from which a track localization efficiency higher than 50% and a contamination of 2% from wrong associations are expected. These expectations are based on the requirement that only one candidate track is found in the scanning area of all three emulsion trackers. Scanning and measurement in the emulsion sheets is performed by an automatic microscope.

The relative distance between tracks of candidate events and reference tracks is measured with an accuracy of ~5 μm in each of the three emulsion sheets traversed. The reference tracks are those of beam-associated muons, for which the momenta are measured by the muon spectrometer to be higher than 30 GeV/c. Alignment muon tracks, recorded outside the normal neutrino data taking periods with the air-core magnet off, are well suited as reference tracks. By combining the information in the three emulsion trackers, the momentum of candidate hadrons can be precisely measured. Depending on the quality of the reference track, the momentum resolution σ_p/p ranges from 22% at 10 GeV/c to between 26% and 37% at 30 GeV/c.

15. Status of the experiment

The CHORUS experiment was approved in September 1991 by the CERN SPSLC Committee. The construction of the detector was completed by November 1993 when a technical run with a passive dummy target was conducted. Physics data taking with the complete emulsion target started in May 1994. After the 1994 run, one of the four emulsion stacks (200 kg in mass) was processed to allow the first physics analysis to start. The remaining three stacks were stored underground during the long annual shutdown.

Data taking resumed in April 1995 with the three old stacks together with one new stack. All four stacks were processed after the completion of the run in October 1995. The experiment was then approved to continue data taking in 1996–1997, using new emulsion stacks. At the completion of the 1996 run, all four emulsion stacks were stored underground and will be used again in the 1997 run.

A summary for the CHORUS 1994–1996 runs is given in Table 3, showing the number of 450 GeV protons delivered to the beryllium target to produce the neutrino beam, the CHORUS detector efficiency (duty cycle), the number of main-trigger events recorded, and the expected number of ν_μ charged-current events in the emulsion target.

The CHORUS apparatus has been fully operational with excellent performance since the beginning of data taking. A typical ν_μ charged-current event recorded by the detector is depicted in Fig. 35, showing the muon final-state and the associated hadronic shower. First physics results have been reported [33],

Table 3
Summary of the CHORUS runs in 1994–1996

	1994	1995	1996
SPS Proton on target (/ 10^{19})	0.81	1.20	1.38
Detector efficiency	77%	88%	94%
"Main" triggers recorded	422 k	547 k	620 k
Expected ν_μCC events in emulsion	120 k	200 k	230 k

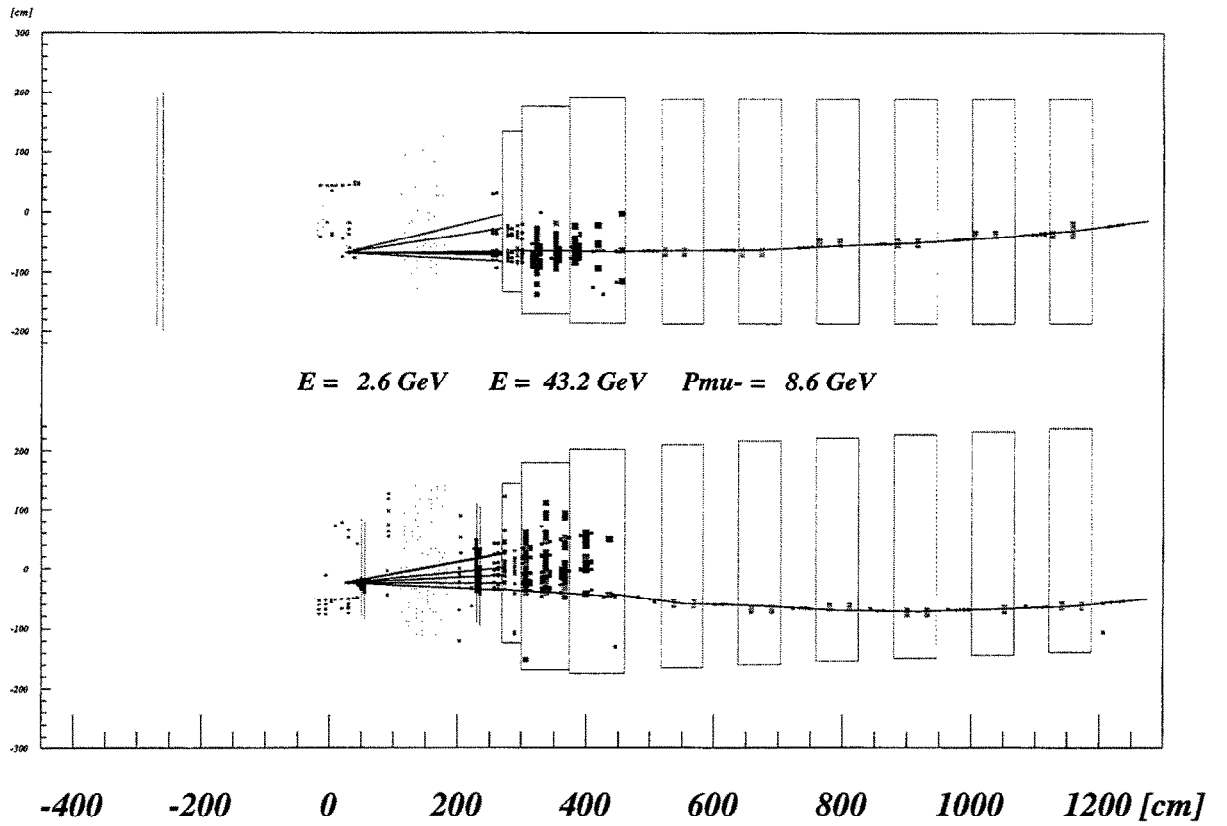

Fig. 35. A typical charged-current neutrino-induced event recorded in the CHORUS detector.

demonstrating that the experiment as a whole works according to expectation, and the sensitivity aimed at can be achieved.

16. Conclusions

The aim of the CHORUS experiment at CERN is a high sensitivity search for $\nu_\mu \rightarrow \nu_\tau$ oscillation in the SPS Wide Band Neutrino Beam. The CHORUS apparatus has been successfully constructed and commissioned on schedule, and excellent operational conditions have been obtained. The experiment design includes several novel and challenging features: the largest emulsion system exposed for the longest duration, the largest scintillating fiber tracker and the first large scale "spaghetti" calorimeter, as well as new development in the technique of emulsion scanning by means of automatic microscopes.

The expected hardware performance of the different detectors have been achieved, and the first physics results indicated that the designed sensitivity is within reach. The performance of the apparatus with the neutrino beam will be the subject of a forthcoming publication.

Acknowledgements

The realization of the CHORUS experiment was possible thanks to the skill and dedication of the many people who contributed to the various aspects. We wish to express our deep appreciation to the numerous engineers and technical collaborators from the participating institutes who took part in the realization of the different subdetectors and to their assembly and test.

In particular we wish to thank: D. Bourillot, A. Decoster, M. De Schutter, J. Domeniconi,

J. Dupont, J. Dupraz, J.L. Garavel, R. Gindroz, H. van Heynitz, A. van Hove, T. Kawai, H. Ishikawa, P. Lamonte, D. Luypaert, P. Nappey, F. Peron, M. Pins, R. Pins, R. Pintus, E. Raspoet, S. Reynaud, G. Roiron, R. Ruidant, G. Van Beek and G. Vincent for their help with the construction, installation and test of the scintillating fiber trackers and of the associated optoelectronics; V. Carassiti for the technical design of the calorimeter together with G. Basti and G. Passeggio; S. Bigoni, G. Bonora, M. Borriello, C. Farella, R. Gorini, A. Iaciofano, G. Improta, V. Marzullo, M. Melchiorri, F. Pagano, L. Parascandolo and R. Rocco for their contribution to the realization of the calorimeter; A. Jokhov, A. King, A. Outenkov and M. Ryabinin for their work on the muon spectrometer; J. André, S. Fahnauer, P.A. Guidici, M. Löbe, K. Mühlemann, G. Petrucci, D. Rotil, A. Schwarz and M. Wegener for general engineering; F. Bal, C. Bonnet, S. Cairanti, E. Falk, M. Ferrat, F. Formenti, C. Millerin and L. Thibaudeau for their contributions to the detector electronics; J.P. Dewulf for his work on the trigger system; C. Rosset for his work on the emulsion target support structure; F. Cataneo for his contribution to the slow control system; B. Friend and A. Guerriero for their work on the data acquisition system; M. van Beuzekom for design and engineering part of the trigger logic as well as for design of the honeycomb tracker electronics, with contributions from E.A. van den Born, P.P.M. Jansweijer, J.D. Schipper and J. Stolte; J.P.M. Buskens, H. van der Graaf, H. Kok, J.P.M. Metselaar for the mechanical design and realisation of the honeycomb chambers; C. Sgarbi for the software management and the excellent organization of the Rome scanning laboratory and A. Andriani, R. Diotallevi, P. Dipinto, V. Dipinto, F. Fiorello, M. Jeanrenaud and G. Mentes for their contribution to the emulsion laboratory and scanning facilities; S. Anthony, C. Gentet and H. Gruber for general support.

We are also indebted to the SPS staff and in particular to V. Falaleev and to the group of J.M. Maugain for the efficient neutrino beam operation, and to L. Gatignon for the West Area test beams, C. Lasseur and the CERN survey group. The general technical support from the PS, SPS, ECP and CN Divisions is warmly acknowledged.

We gratefully acknowledge the financial support of the different funding agencies: in particular, the Institut Interuniversitaire des Sciences Nucleaires and the Interuniversitair Instituut voor Kernwetenschappen (Belgium), the Israel Science Foundation (grant 328/94) and the Technion Vice President Fund for the Promotion of Research (Israel), the German Bundesministerium für Bildung und Forschung under contract numbers 05 6BU11P for Berlin and 05 7MS12P for Münster, the Istituto Nazionale di Fisica Nucleare (Italy), the Japan Private School Promotion Foundation and Japan Society for the Promotion of Science (Japan), the Korea Science and Engineering Foundation, and the Ministry of Education through Research Fund (BSRI-96-2407) (Republic of Korea), the foundation for fundamental research on matter FOM and the national scientific research organisation NWO (the Netherlands), the Scientific and Technical Research Council of Turkey (TUBITAK).

References

[1] For an overview on the subject of neutrino physics, see, e.g., K. Winter (Ed.), Neutrino Physics, Cambridge University Press, 1991.

[2] For the current status of neutrino physics, see, e.g., M. Roos (Ed.,) Proc. XVII Int. Conf. on Neutrino Physics and Astrophysics, Helsinki 1996, World Scientific, 1996.

[3] H. Harari, Phys. Lett. B 216 (1989) 413.

[4] N. Armenise et al., CHORUS Proposal, CERN-SPSC/90-42, 1990;
M. de Jong et al., CERN-PPE/93-131, 1993.

[5] N. Ushida et al., Phys. Rev. Lett. 57 (1986) 2897;
M. Gruwé et al., Phys. Lett. B 309 (1993) 463;
K.S. McFarland et al., Phys. Rev. Lett. 75 (1995) 3993;
P.F. Loverre, Phys. Lett. B 370 (1996) 156.

[6] Ya. B. Zel'dovich, I.D. Novikov, Relativistic Astrophysics, Nauka, Moscow, 1967;
J. Ellis, J.L. Lopez, D.V. Nanopoulos, Phys. Lett. B 292 (1992) 189;
H. Fritzsch, D. Holtmannspötter, Phys. Lett. B 338 (1994) 290.

[7] P. Astier et al., NOMAD Proposal, CERN-SPSLC/91-21 (1991); Addendum CERN-SPSLC/91-48; and Addendum CERN-SPSLC/91-53.

[8] E. Heijne, CERN Yellow Report 83-06, 1983;
G. Acquistapace et al., CERN Preprint, CERN-ECP/95-14, 1995.

[9] L. Casagrande et al., CERN Yellow Report 96-06, 1996.

[10] S. Sorrentino, Laurea Thesis, Università "Federico II", Naples, 1995;

B. Van de Vyver, Nucl. Instr. and Meth. A 385 (1997) 91; M.C. Gonzalez-Garcia, J.J. Gomez-Cadenas, CERN-PPE/96-114, 1996.

[11] D. Geiregat et al., CHARM II Collaboration, Phys. Lett. B 232 (1989) 539;
P. Vilain et al., CHARM II Collaboration, Phys. Lett. B 281 (1992) 159.

[12] N. Ushida et al., Nucl. Instr. and Meth. 224 (1984) 50; S. Aoki et al., Nucl. Instr. and Meth. A 274 (1989) 64; K. Kodama et al., Nucl. Instr. and Meth. B 93 (1994) 340.

[13] S. Aoki et al., Nucl. Instr. and Meth. B 51 (1990) 446.

[14] S. Aoki et al., Nucl. Instr. and Meth. A 344 (1994) 143; P. Annis et al., Nucl. Instr. and Meth. A 367 (1995) 367; P. Annis et al., Nucl. Instr. and Meth., in preparation.

[15] T. Nakano et al., in: Proc. IEEE Nuclear Science Symp., Santa Fe, 1991;
T. Nakano et al., in: Proc. Scintillating Fiber Symp., SCIFI '93, University of Notre Dame, 1993.

[16] M. Gruwé, Ph.D. Thesis, Université Libre de Bruxelles, 1994; D. Rondeshagen, Dipl. Thesis, Westfälische Wilhelms-Universität, 1994;
C. Mommaert, Ph.D. Thesis, Vrije Universiteit Brussel, 1995.

[17] F. Bergsma et al., Nucl. Instr. and Meth. A 357 (1994) 243.

[18] D. Acosta et al., Nucl. Instr. and Meth. A 308 (1991) 481.

[19] S. Buontempo et al., Nucl. Instr. and Meth. A 349 (1994) 70.

[20] L. Gatignon, CERN SL/Note 95-72 (EA), 1995.

[21] E. Di Capua et al., Nucl. Instr. and Meth. A 378 (1996) 221.

[22] H. Abramovitz et al. (CDHS Collaboration), Nucl. Instr. and Meth. 180 (1981) 429;
A. Blondel et al. (CDHS Collaboration), Z. Phys. C 45 (1990) 361.

[23] J.P. Dewulf et al. (CHARM II Coll.), Nucl. Instr. and Meth. A 252 (1986) 443;
J.P. Dewulf et al. (CHARM II Coll.), Nucl. Instr. and Meth. A 263 (1988) 109;
D. Geiregat et al. (CHARM II Coll.), Nucl. Instr. and Meth. A 325 (1993) 92;
T. Bauche, Ph.D. Thesis, University of Hamburg, 1988.

[24] G. Marel et al., Nucl. Instr. and Meth. 141 (1977) 43; M. Holder et al. (CDHS Collaboration), Nucl. Instr. and Meth. 148 (1978) 235.

[25] T. Patzak, Ph.D. Dissertation, Humboldt University of Berlin, 1995.

[26] G. Carnevale et al., in: Proc. CHEP '94 Conf., 101, San Francisco, 1994;
F. Riccardi, Ph.D. Thesis, Università "Federico II", Naples, 1996.

[27] Slow Control – D. Bonekämper, Dipl. Thesis, Westfälische Wilhelms-Universität, 1995.

[28] K. Hoshino, G. Rosa, Nuclear Tracks 12 (1986) 477.

[29] T. Nakano, Ph.D. Thesis, Nagoya University, 1997;
G. Rosa et al., Preprint Salerno University DSF US 1/97, Nucl. Instr. and Meth., submitted.

[30] G. Fiorillo, Ph.D. Thesis, Università "Federico II", Naples, 1995.

[31] H. van der Graaf et al., Nucl. Instr. and Meth. A 307 (1991) 220.

[32] RASNIK system: ATLAS technical proposal, CERN/LHCC/94-33, 1994, p. 131.

[33] K. Niwa (CHORUS Collaboration), in: M. Roos (Ed.), Proc. XVII Int. Conf. on Neutrino Physics and Astrophysics, Helsinki 1996, World Scientific, 1996;
C. Weinheimer (CHORUS Collaboration), in: A. Wróblewski (Ed.), Proc. Int. Conf. on High Energy Physics, Warsaw 1996, World Scientific, 1996.